Monthly Notices of the ROYAL ASTRONOMICAL SOCIETY

MNRAS **499,** 3320–3337 (2020) doi:10.1093/mnras/staa2909
Advance Access publication 2020 September 23

J-factor estimation of Draco, Sculptor, and Ursa Minor dwarf spheroidal galaxies with the member/foreground mixture model

Shun-ichi Horigome [1]★ Kohei Hayashi [1,2] Masahiro Ibe,[1,2] Miho N. Ishigaki,[3] Shigeki Matsumoto[1] and Hajime Sugai[1]

[1]*Kavli Institute for the Physics and Mathematics of the Universe (Kavli IPMU, WPI), The University of Tokyo, Chiba 277-8583, Japan*
[2]*Institute for Cosmic Ray Research (ICRR), The University of Tokyo, Chiba 277-8583, Japan*
[3]*Astronomical Institute, Tohoku University, Aoba-ku, Sendai 980-8578, Japan*

Accepted 2020 September 16. Received 2020 August 24; in original form 2020 February 12

ABSTRACT

Dwarf spheroidal galaxies (dSphs) are promising targets of indirect detection experiments searching for dark matter (DM) at present Universe. Towards robust prediction for the amount of signal flux originating in DM annihilation inside dSphs, a precise determination of DM distributions as well as *J*-factors of the dSphs is particularly important. In this work, we estimate those of Draco, Sculptor, and Ursa Minor dSphs by an improved statistical method in which both foreground stars and dSph member stars are simultaneously taken into account. We define the likelihood function of the method as the so-called conditional one to remove sampling bias of observed stellar data. This improved method enables us to estimate DM distributions and *J*-factors of the dSphs directly from observed stellar data contaminated by foreground stars without imposing stringent membership criteria on the measured quantities.

Key words: astroparticle physics – instrumentation: spectrographs – galaxies: dwarf – dark matter – gamma-rays: galaxies.

1 INTRODUCTION

The existence of dark matter (DM) in our universe was strongly confirmed by various astrophysical observations such as dynamics of galaxy clusters (Zwicky 1933), rotation curves of galaxies (Rubin, Thonnard & Ford 1978; Rubin, Ford & Thonnard 1980), and gravitational lensing (McLaughlin 1999; Bradac et al. 2006; Clowe et al. 2006). The global analysis of cosmic microwave background, large-scale structure and supernovae observation data (Ade & others 2016) tells us that DM is responsible for a quarter of the total energy of the present universe; however, the microscopic nature of DM is still unknown. Weakly interacting massive particle (WIMP) is an attractive DM candidate, which can naturally explain DM abundance observed today by the well-established freeze-out mechanism. In particular, WIMP with TeV scale mass is well motivated from the viewpoint of new physics beyond the standard model of particle physics (Moroi & Randall 2000; Hisano et al. 2007; Evans et al. 2013; Bhattacherjee et al. 2014), and the WIMP is, in fact, intensively studied after the discovery of the Higgs boson at the Large Hadron Collider experiment.

The most promising way to detect the WIMP is the indirect detection searching for signal from DM rich region. Among various targets of the detection, dwarf spheroidal galaxies (dSphs) associated with the Milky Way are ideal ones, as they contain a large amount of DM with small astrophysical backgrounds (Cholis & Salucci 2012; Lefranc et al. 2016) and are located, at most, a few hundred kpc away from our Solar system. In fact, the gamma-ray search from dSphs excluded a typical WIMP with the mass less than 100 GeV (Ackermann et al. 2015). The signal flux of the detection depends not only on the particle nature of DM but also on an astrophysical factor concerning the dSph, namely the *J*-factor:

$$J(\Delta\Omega) = \left[\int_{\Delta\Omega} \mathrm{d}\Omega \int_{\mathrm{l.o.s.}} \mathrm{d}l\, \rho^2_{\mathrm{DM}}(l,\ \Omega)\right] . \quad (1)$$

Here, we define a DM density profile at a distance l and an angle Ω by $\rho_{\mathrm{DM}}(l,\ \Omega)$, which is estimated by the comparison between the observed velocity dispersion curve of dSph member stars and the theoretical prediction on the dispersion curve from dSph stellar kinematics. It is, however, known that several uncertainties are associated with the estimation: spatially dependent anisotropy of the dispersion (Ullio & Valli 2016; Read & Steger 2017; Read, Walker & Steger 2018; Alvarez et al. 2020), non-spherical profile (Bonnivard et al. 2015; Hayashi et al. 2016), size of halo truncation (Geringer-Sameth, Koushiappas & Walker 2015), contamination of binary stars (Koch et al. 2007; Simon & Geha 2007; Mateo, Olszewski & Walker 2008), prior bias of Bayesian analysis (Martinez et al. 2009), and foreground contamination (Bonnivard, Maurin & Walker 2016; Ichikawa et al. 2017, 2018).

In particular, it is necessary to take care of the foreground contamination even for the case of future observations yielding a larger amount of observational data, because the number of foreground stars contributing to the contamination increases along the amount of the data. Various methods are adopted in conventional analyses to remove contaminating stars such as simple sigma-clipping procedure (Coleman, Da Costa & Bland-Hawthorn 2005),

★ E-mail: shunichi.horigome@ipmu.jp

© 2020 The Author(s)
Published by Oxford University Press on behalf of the Royal Astronomical Society

Downloaded from https://academic.oup.com/mnras/article/499/3/3320/5910521 by guest on 23 April 2024

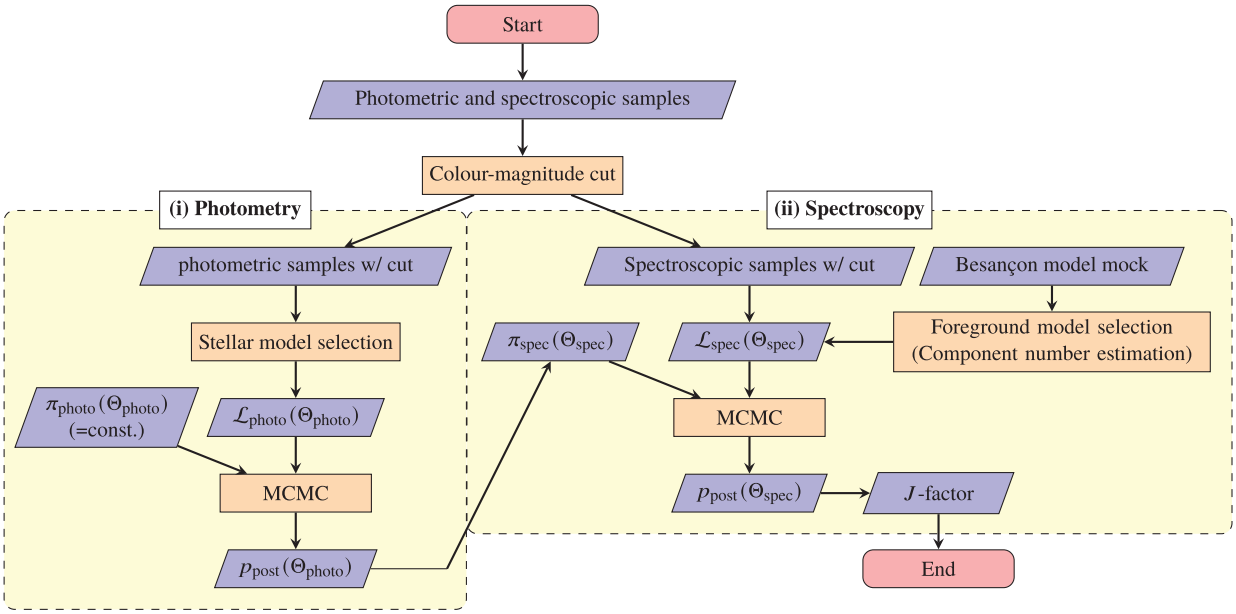

Figure 1. Flow chart of our analysis method. See Section 2 for more details.

membership selection based on the expectation-maximization (EM) algorithm (Walker et al. 2009b), and full Bayesian analysis with the foreground model of a single Gaussian component (Bonnivard et al. 2016). In Ichikawa et al. (2017), hereafter KI, 2018), we have investigated the effect of the foreground contamination on the *J*-factor estimations of classical and ultrafaint dSphs. One of the goals of our papers was to develop observational strategies and analysis methods for future instruments such as the prime focus spectrograph (PFS) mounted on the 8.2-m Subaru Telescope.PFS is the next-generation spectrograph of the SuMIRe project (Takada et al. 2014; Sugai et al. 2015; Tamura et al. 2016) with a large field of view (∼1.38 deg diameter) and about 2400 fibres, which allows us to observe not only member-like stars but also many foreground stars simultaneously. We have defined a likelihood function based on the mixture model of a dSph member component and three foreground components motivated by the fitting of the Besançon model (Robin et al. 2003). Using our constructed likelihood function, we have demonstrated that the likelihood function can successfully reproduce the input parameters of mock observational data thanks to large data sets yielded by the large field of view of PFS. By contrast, membership selection based on the EM algorithm can result in biased *J*-factor estimation when the intrinsic velocity dispersion is not flat. Moreover, the selection method sometimes suffers from the foreground contamination effect because even a few contaminating stars located at the outer region of a dSph make us overestimate the velocity dispersion.

When we apply KI's method to the actual data sets, we, however, need to treat spatial sampling biases of the observed data (Martinez et al. 2011) because the surface density of observed spectroscopic data is not equal to the actual surface density of a dSph due to the sampling. Therefore, in this work, we improve the mixture model likelihood developed in KI to deal with actual stellar data with the sampling biases. Using this improved likelihood function, we obtain the non-biased *J*-factors of Draco, Sculptor, and Ursa Minor dSphs robustly in terms of the foreground contamination.

The organization of this paper is as follows: In Section 2, we describe our analysis method, which is separated into two parts, photometric and spectroscopic parts. We define likelihood functions for these two parts in Sections 2.1 and 2.2, respectively. In Section 2.3, we discuss a sampling algorithm to obtain posterior probability density functions of model parameters as well as the *J*-factor. In Section 3.1, we introduce photometric and spectroscopic data sets for each dSph used in our analysis. In Sections 3.2 and 3.3, we explain the pre-processing for the data introduced in the previous subsection. In Section 4, we show our results of parameter estimation and *J*-factor posteriors. In Section 5, we discuss the results of our estimation. We summarize our discussion in Section 6.

2 METHODS

We first show the flowchart of our analysis method in Fig. 1. Our method is mainly separated into two parts as follows:

(i) **Photometry**: We make use of up-to-date wide-field, multiband, photometric samples that are available in the public data releases of Sloan Digital Sky Survey (Abolfathi et al. 2018), Pan-STARRS (Chambers et al. 2016), and Dark Energy Survey (Abbott et al. 2018). For each dSph, we impose a colour–magnitude cut on the photometric samples to stand out member star candidates on data. With the use of these candidates, we select a suitable stellar density profile from two empirical spatial profiles shown in equation (5) by comparing their statistical evidence. We then estimate the half-light radius and the local membership probability at this radius.

(ii) **Spectroscopy**: We compile the largest samples of stellar line-of-sight velocities that are available from references Walker, Olszewski & Mateo (2015, 2009a) and Spencer et al. (2018). Before going to the spectroscopic analysis, we fix the number of independent components of foreground stars by comparing velocity distributions of the data set and of the Besançon model. Using photometric information (i.e. magnitude of each band) taken from the spectroscopic samples, we impose the same colour–magnitude cut on the spectroscopic samples to avoid sampling bias in terms of colour–magnitudes between the photometric and spectroscopic samples. After that, we estimate the DM halo parameters, and evaluate the posterior distribution of the *J*-factor based on the line-of-

Downloaded from https://academic.oup.com/mnras/article/499/3/3320/5910521 by guest on 23 April 2024

Table 1. Photometric and spectroscopic data, where $r_{\rm max}$ is the radius of the outermost star Geringer-Sameth et al. (2015). See Section 3.1 for more details.

dSph	Photometry	$R_{\rm photo}$ (deg)	Spectroscopy	$r_{\rm max}$ (pc)
Draco	SDSS DR14 (Abolfathi et al. 2018)	1.0	MMT/Hectochelle (Walker et al. 2015)	1866
Sculptor	DES DR1 (Abbott et al. 2018)	2.5	Magellan/MMFS (Walker et al. 2009a)	2673
Ursa Minor	Pan-STARRS DR1 (Chambers et al. 2016)	2.0	MMT/Hectochelle (Spencer et al. 2018)	1580

sight velocities. We use the posterior parameter distributions of the half-right radius and the local membership probability obtained from the photometric analysis as prior distributions of the spectroscopic analysis.

Here, it is worth emphasizing that imposing the same criteria on the colour–magnitude for both the photometry and the spectroscopic data means that the membership probability that is tightly fixed to be a specific value by the photometric analysis can be directly applied to the membership probability in the spectroscopic analysis. In addition, we also take the other uncertainty into account in our analysis, which is from the distance between dSph and our Solar system. As shown in Appendix C, the value of the J-factor is scaled as $J_D \to J_{kD} = k^{-3} J_D$ under the scaling of $D \to kD$ with D being the distance, and hence it can cause a large uncertainty on the J-factor estimation. Note that this scaling of the J-factor is always held whenever we adopt the spherical Jean-analysis.

We explain each step of our analysis method in more details in the rest of this section assuming following conditions:

(i) The foreground stars are assumed to be uniformly distributed inside the celestial sphere around the region of interest (RoI).

(ii) The velocity distribution of the foreground stars is composed of at most up to three components, which are corresponding to the thin disc, thick disc, and halo components, respectively. Note again that the number of the components for foreground stars is fixed at the step of the model selection in the spectroscopic part (Section 2.2).

(iii) The velocity distribution of each foreground component mentioned above is described by a Gaussian distribution.

(iv) Spectroscopic samples are randomly selected, meaning that the photometric samples and the spectroscopic ones originate from an identical statistical population, after the colour–magnitude cut.

(v) The velocity distribution of the member stars does not depend on their colour–magnitudes.

For the discussion of the validity of assumption (iv) and (v), see Appendix B.

2.1 Photometry

The purpose of this photometric part is to determine stellar profiles (shapes and half-light radii) of the dSphs and membership probabilities at the half-light radii using photometric samples, which will be further used in the subsequent spectroscopic analysis.

2.1.1 *Likelihood function*

The half-light radius of the stellar distribution of a dSph and the membership probability at this radius is estimated using the following set-up of the likelihood function $\mathcal{L}_{\rm photo}$ and prior $\pi_{\rm photo}$:

$$\mathcal{L}_{\rm photo}(\Theta_{\rm photo}) = \prod_i 2\pi R_i [s\mathcal{N}_1 \Sigma_1(R_i) + (1-s)\mathcal{N}_0 \Sigma_0(R_i)] \,, \quad (2)$$

$$\pi_{\rm photo}(\Theta_{\rm photo}) : \text{flat}. \quad (3)$$

Here, $\Theta_{\rm photo}$ is the parameter set of the photometry model (to be mentioned later) and R_i denotes the projected radius given by $R_i = D\sin\theta_i$, where θ_i is the separation angle of the ith star from the centre of the dSph distant by D from the Earth. $\Sigma_M(R)$ denotes the projected stellar profile of dSph member stars ($M = 1$) and foreground stars ($M = 0$). As stated above, we take $\Sigma_0(R) = $ const. The normalization factor $\mathcal{N}_M$ is given by the equation $\mathcal{N}_M \equiv (\int_0^{R_{\rm photo}} {\rm d}R 2\pi R \Sigma_M(R))^{-1} < 1$ for each $\Sigma_M(R)$, where the integration is performed from the centre ($R = 0$) to the maximum radius of the photometric stars denoted by $R_{\rm photo}$. See also Table 1. The coefficient s stands for the global membership probability of the dSph, which is given by the following formula:[1]

$$s = [1 + \frac{1}{{\rm Odds}(R_{1/2})} \frac{\mathcal{N}_1 \Sigma_1(R_{1/2})}{\mathcal{N}_0 \Sigma_0(R_{1/2})}]^{-1} \,. \quad (4)$$

Here, $R_{1/2} \equiv D\sin\theta_{1/2}$ denotes the half-light-radius of the dSph with $\theta_{1/2}$ being the corresponding separation angle, while ${\rm Odds}(R_{1/2})$ is the odds of the membership at the half-light-radius. The odds is given by $P(M = 1|R = R_{1/2})/P(M = 0|R = R_{1/2})$, where $P(M|R)$ is the local membership probability at a specific radius R. Here, we note that the parameter D disappear in the photometric likelihood function because D does not depend on i. As a result, the likelihood function $\mathcal{L}_{\rm photo}$ has four independent parameters: $\Theta_{\rm photo} = \alpha_0$, δ_0, $\theta_{1/2}$, ${\rm Odds}(R_{1/2})$, where α_0 and δ_0 are the right ascension and declination of the centre of the dSph.

2.1.2 *Stellar model selection*

We consider the following two empirical stellar profiles in our analysis; Plummer profile (Plummer 1911) and Exponential profile:

$$\Sigma_1(R) = \begin{cases} \dfrac{1}{\pi R_{1/2}^2}[1 + (R/R_{1/2})^2]^{-2} & \text{(Plummer profile)} \\ \dfrac{1}{2\pi R_{\rm e}^2}\exp(-R/R_{\rm e}) & \text{(Exponential profile)} \end{cases} , \quad (5)$$

where R denotes the projected distance from the centre of a dSph, and $R_{\rm e}$ denotes the exponential radius scale, corresponding to $R_{1/2} = 1.68R_{\rm e}$. These two profiles can fit observed stellar profiles of the dSphs very well (Irwin & Hatzidimitriou 1995; Ségall et al. 2007; Martin, de Jong & Rix 2008). Those can be analytically de-projected into the three-dimensional stellar number density $\nu_1(r)$ as

$$\nu_1(r) = \begin{cases} \dfrac{3}{4\pi R_{1/2}^3}[1 + (r/R_{1/2})^2]^{-5/2} & \text{(Plummer profile)} \\ \dfrac{1}{2\pi^2 R_{\rm e}^3} K_0(r/R_{\rm e}) & \text{(Exponential profile)} \end{cases} , \quad (6)$$

[1] In KI, the coefficient s is used as one of parameters of the likelihood function even in the spectroscopic analysis. The value of s, however, depends on the maximum radius of the photometric samples. Furthermore, the area of the spectroscopic observation is usually not even a circle but a combination of some irregular ones, which complicates the calculation of the global membership probability. See Appendix A for more details.

Downloaded from https://academic.oup.com/mnras/article/499/3/3320/5910521 by guest on 23 April 2024

where r denotes the distance from the centre of a dSph. $K_0(x)$ is the modified Bessel function of the second kind. Note also that the stellar number density is normalized to be $\int \mathrm{d}r\, 4\pi r^2\, \nu_1(r) = 1$, so as the projected one, namely $\int \mathrm{d}R\, 2\pi R\, \Sigma_1(R) = 1$.

In our analysis, we select the most probable model among the two based on the Bayes factor, namely the ratio of statistical evidences. The statistical evidence of a specific model is defined by the integral of the likelihood function times the prior distribution $\int \mathrm{d}\Theta \mathcal{L}(\Theta)\pi(\Theta)$, which corresponds to the mean likelihood value of the hypothesis for a given data set. Although the integration of $\int \mathrm{d}\Theta \mathcal{L}(\Theta)\pi(\Theta)$ is difficult due to large dimensions of Θ, several techniques are developed to evaluate this integration. In this work, we use the Markov Chain Monte Carlo (MCMC) technique to evaluate statistical evidences, as discussed in Section 2.3.

2.2 Spectroscopy

The purpose of this part is to determine DM density profile and J-factor of a dSph using the results of the previous part as priors.

2.2.1 Foreground model selection

We assume up to three Gaussian components for the Milky Way contamination (the foreground contribution) as already mentioned, namely the thin disc, thick disc, and halo components. In the actual data sample, however, not all of those components are appreciable due to the contribution from a dSph. Hence, in order to determine the number of foreground components in advance, we refer the Besançon model[2] (Robin et al. 2003). We first generate the mock stars according to the model, where the number of generated stars is determined, so that it becomes compatible with the actual data. Then, we compare the statistical evidences of N-component foreground models (N = 1, 2, 3) and adopt the most likely one.

2.2.2 Stellar velocity dispersion and DM density profile

DM density profiles of dSphs are estimated by comparing observed data of line-of-sight velocity dispersion with theoretical predictions. Assuming that dSphs are spherical and steady systems, dispersion curves of the dSphs are predicted by the following spherical Jeans equation (Binney & Tremaine 2008):

$$\frac{1}{\nu_1(r)}\frac{\partial \nu_1(r)\sigma_r^2(r)}{\partial r} + \frac{2\beta_{\rm ani}(r)\sigma_r^2(r)}{r} = -\frac{GM(r)}{r^2}\,. \tag{7}$$

Here, G is the gravitational constant and $M(r)$ is the enclosed mass within r, which is given by $M(r) = \int_0^r \mathrm{d}r' 4\pi r'^2 \rho_{\rm DM}(r')$ for the case of a dSph due to the fact that the mass is dominated by DM contribution. The velocity dispersion of member stars are defined by σ_r, σ_θ, and σ_ϕ in general, which denote the dispersion along the radial, polar, and azimuthal directions, respectively. Now, we can take $\sigma_\theta = \sigma_\phi$ because of the spherical symmetry, while the anisotropy parameter $\beta_{\rm ani}$ is defined to be $\beta_{\rm ani} \equiv 1 - (\sigma_\theta^2 + \sigma_\phi^2)/(2\sigma_r^2)$.

We obtain the line-of-sight velocity dispersion $\sigma_{\rm los}^2(R)$ of dSph member stars by solving the Jeans equation under the assumption of a constant anisotropy parameter $\beta_{\rm ani}(r) = \beta_{\rm ani}$,

$$\sigma_{\rm los}^2(R) = \frac{2}{\Sigma_1(R)}\int_R^\infty \mathrm{d}r\left(1 - \beta_{\rm ani}\frac{R^2}{r^2}\right)\frac{\nu_1(r)\sigma_{\rm r}^2(r)}{\sqrt{1 - R^2/r^2}}\,, \tag{8}$$

[2] https://model.obs-besancon.fr/modele_simuls.php

where the velocity dispersion along the radial direction $\sigma_{\rm r}$ is

$$\sigma_{\rm r}^2(r) = \frac{1}{\nu_1(r)}\int_r^\infty \nu_1(r')\left(\frac{r'}{r}\right)^{2\beta_{\rm ani}}\frac{GM(r')}{r'^2}\mathrm{d}r'\,. \tag{9}$$

Here, we assume the generalized NFW halo profile (Hernquist 1990; Dehnen 1993; Zhao 1996) for the DM density profile,

$$\rho_{\rm DM}(r) = \rho_{\rm s}(r/r_{\rm s})^{-\gamma}(1 + (r/r_{\rm s})^\alpha)^{-(\beta-\gamma)/\alpha}, \tag{10}$$

where parameters $\rho_{\rm s}$ and $r_{\rm s}$ are the scale density and the scale radius of the DM density profile, respectively, while other parameters α, β, and γ determine the shape of the profile. For instance, $(\alpha,\ \beta,\ \gamma) = (1,\ 3,\ 1)$ gives the famous Navarro–Frenk–White (NFW) profile (Navarro, Frenk & White 1997), while $(\alpha,\ \beta,\ \gamma) = (1.5,\ 3,\ 0)$ (approximately) gives the Burkert profile (Burkert 1995).

2.2.3 Likelihood function and prior

In KI, the likelihood function is defined by the mixture model of dSph member stars and foreground stars, as explicitly shown in Appendix A, which is based on the simultaneous probability density $P(v,\ R)$ with v and R being the stellar line-of-sight velocity and the radius from the centre of the dSph, respectively. The likelihood function is indeed proved to successfully reproduce original input parameters by analysis using mock data, as was shown in KI.

To analyse actual observed data, however, we should consider the spatial sampling bias of observed stars (Martinez et al. 2011). We therefore use a improved likelihood function for spectroscopic samples based on the conditional probability $P(v|R) = P(v,\ R)/\int \mathrm{d}R P(v,\ R)$ rather than $P(v,\ R)$ itself:

$$\mathcal{L}_{\rm spec}(\Theta_{\rm spec}) = \prod_i \Bigg[s(R_i)\mathcal{G}[v_i; v_1, \sqrt{\sigma_1^2(R_i) + \delta\sigma_i^2}] + [1 - s(R_i)]\sum_{\rm c}\pi_{\rm c}\mathcal{G}[v_i; v_{0,\rm c}, \sqrt{\sigma_{0,\rm c}^2 + \delta\sigma_i^2}]\Bigg], \tag{11}$$

where $\mathcal{G}[v; \mu, \sigma]$ is the Gaussian function whose mean and standard deviation are given by μ and σ, respectively. Here, $\delta\sigma_i$ is the observational error of the ith star.[3] The mean velocity of member stars are denoted by v_1, while the velocity dispersion of the stars is $\sigma_1(R)$, which is nothing but $\sigma_{\rm los}(R)$ defined in equation (8). On the other hand, $v_{0,\rm c}$, $\sigma_{0,\rm c}$, and $\pi_{\rm c}$ denote the mean velocity, velocity dispersion, and weight of the cth foreground component, respectively, where the coefficients $\pi_{\rm c}$ are normalized to be $\sum_c \pi_c = 1$. At last, $s_{\rm R}$ denotes the local membership probability of stars at the radius R (see also Appendix A), which is given as follows:

$$s(R) = \left[1 + \frac{1}{\mathrm{Odds}(R_{1/2})}\frac{\Sigma_1(R_{1/2})/\Sigma_1(R)}{\Sigma_0(R_{1/2})/\Sigma_0(R)}\right]^{-1}. \tag{12}$$

Parameters of the spectroscopic likelihood function are $\Theta_{\rm spec} = \Theta_{\rm photo} \cup r_s,\ \rho_s,\ \alpha,\ \beta,\ \gamma,\ \beta_{\rm ani},\ D,\ v_1 \cup_{\rm c} \pi_{\rm c},\ v_{0,\rm c},\ \sigma_{0,\rm c}$. Here, we should note that the number of independent parameters are $|\Theta_{\rm spec}| - 1$ due to $\sum_{\rm c}\pi_{\rm c} = 1$, e.g. we have $4 + 8 + 3 \times 3 - 1 = 20$ independent parameters for the three-component foreground model.

We introduce Gaussian, flat, log-flat priors for these parameters: We consider Gaussian priors, $\pi(\Theta_{\rm photo}) = \mathcal{G}[\Theta; \mu_\Theta, \sigma_\Theta]$ and

[3] In KI, we ignored this observational error because it does not cause significant difference in J-factor estimation. However, we find that this term improves the performance of the MCMC because the singularity of the likelihood function at $\sigma_{0,\rm c} \to 0$ can be removed by introducing $\delta\sigma_i$.

Downloaded from https://academic.oup.com/mnras/article/499/3/3320/5910521 by guest on 23 April 2024

$\pi(D) = \mathcal{G}[D; \mu_{\rm D}, \sigma_{\rm D}]$, for $\Theta_{\rm photo}$ and D, respectively. Here, μ_Θ and σ_Θ is the median and the half of the 68 per cent quantile of the posterior distribution obtained by the statistical analysis in the photometry part mentioned in the previous subsection, while $\mu_{\rm D}$ and $\sigma_{\rm D}$ are the observed distance and its error of a dSph taken from McConnachie (2012). For the DM halo parameters and the anisotropy parameter, we use the flat and log-flat priors over following ranges:

$$\begin{aligned} -4 \leq \log_{10}(\rho_s/[M_\odot {\rm pc}^{-3}]) \leq 4\,, \\ 0 \leq \log_{10}(r_s/[{\rm pc}]) \leq 5\,, \\ 0.5 \leq \alpha \leq 3\,, \\ 3 \leq \beta \leq 10\,, \\ 0 \leq \gamma \leq 1.2\,, \\ -1 \leq -\log_{10}(1-\beta_{\rm ani}) < 1\,, \end{aligned}$$

which are the same as those adopted in Geringer-Sameth et al. (2015). We impose the flat prior for v_1 over the following range:

$$-10^3 < v_1/[{\rm km\ s}^{-1}] < 10^3\,.$$

For the foreground spectroscopic parameters ($\pi_{\rm c}$, $v_{0,\rm c}$ and $\sigma_{0,\rm c}$), we impose flat priors over the following ranges:

$$\begin{aligned} &0 \leq \pi_{\rm c} \leq 1 \text{ with } \pi_1 > \pi_2 > \pi_3 \text{ (see also Section 2.3)}, \\ &-10^4 \leq v_{0,\rm c}/[{\rm km\ s}^{-1}] \leq 10^4\,, \\ &0 \leq \sigma_{0,\rm c}/[{\rm km\ s}^{-1}] \leq 10^4\,. \end{aligned}$$

2.3 Sampling algorithm

Our likelihood functions and posteriors have many parameters. In particular, the spectroscopic one has more than 10 parameters. The MCMC method is known to enable us to generate parameter samples whose distribution satisfies such a multidimensional function. For example, the Metropolis–Hastings algorithm (Metropolis et al. 1953; Hastings 1970) is known as a simple MCMC algorithm. It requires, however, the tuning of hyperparameters, such as the step width and correlation matrix of the random walk in the parameter space. In our study, we use more sophisticated MCMC sampler, the Affine Invariant Ensemble Sampler implemented by `emcee` (Foreman-Mackey et al. 2013), which provides us easy interfaces to make an MCMC code in PYTHON without any hyperparameter tuning except for the step number and the number of *walkers* (parallelized MCMC sampler). We perform parameter samplings with $O(10^6)$ steps using this sampler.

It is important to point out here that the spectroscopic likelihood function has a permutation symmetry that exchanges the foreground components with their parameters (mean, dispersion, and weight). Such a symmetry is known to cause the label-switching problem (Jasra, Holmes & Stephens 2005) by the multimodality of the likelihood function corresponding to the symmetry. Although an additional ordering condition (e.g. $\pi_1 > \pi_2 > \pi_3$, $\mu_1 > \mu_2 > \mu_3$, or $\sigma_1 > \sigma_2 > \sigma_3$) can break the symmetry, these procedures yield accidental local maxima as by-products due to the hard cut-off the parameter space. These local maxima trap a part of the MCMC samplers in low-likelihood regions and distort the shape of the posterior distribution functions. To resolve the problem, we impose the weight ordering condition ($\pi_1 > \pi_2 > \pi_3$) as denoted above and remove MCMC samples trapped around local maxima having significantly small (by the factor of $<10^{-5}$) posterior values.

To evaluate the statistical evidence of each model, we adopt the widely applicable Bayesian information criterion (WBIC) as an approximation of the (minus-log) evidence. The WBIC can be easily computed by MCMC samples and it is valid even for singular model such as Gaussian mixture model (GMM) and our spectroscopic likelihood function (see Appendix D for more details). To evaluate the WBIC, we perform MCMC samplings with $O(10^6)$ steps.

3 DATA

In this section, we discuss the sources of data sets used in our analysis for photometric and spectroscopic samples. We also explain the pre-processing of these data sets, which is also shown in Fig. 2.

3.1 Data sources

The sources of photometric and spectroscopic samples for each dSph are summarized in Table 1. **Photometry**: For Draco, Sculptor, and Ursa Minor, we have referred to SDSS DR14 (Abolfathi et al. 2018), DES DR1 (Abbott et al. 2018), and Pan-STARRS DR1 (Chambers et al. 2016), respectively, to obtain the position (right ascension, declination) and the magnitudes (g, r, i, z, and y bands) of stars. **Spectroscopy**: For Draco, we have used stellar-kinematic samples of MMT/Hectochelle observation (Walker et al. 2015), which provide positions and line-of-sight velocities of the stars. For Sculptor, we have referred to the result of Magellan/MMFS survey (Walker et al. 2009a) to obtain the positions, line-of-sight velocities and V- and I-band magnitudes of the stars. For Ursa Minor, we have obtained the position and velocity data from the observation of MMT/Hectochelle telescope (Spencer et al. 2018).

We have used samples (stars) within the radius $R < R_{\rm photo}$, where $R_{\rm photo} = 1.0\,{\rm deg}$, $2.5\,{\rm deg}$, and $2.0\,{\rm deg}$ for Draco, Sculptor, and Ursa Minor, respectively. We have decided these radii to include both the outermost likely member stars of each dSph and the foreground stars that are sufficient to carry out the multicomponent analysis described in the previous section. Note also that the radii are specifically optimised to ensure that the spatial and velocity distribution of the foreground stars can be assumed to be uniform.

3.2 Cross-matching among photometric and spectroscopic data

To determine the magnitudes of spectroscopic stars, we looked for the closest photometric star on the equatorial coordinates for each spectroscopic star and regard the two stars identical. If the spectroscopic star is located much away from the nearest photometric star (farther than 5 arcsec), it is removed in the spectroscopic analyses.[4]

We note that our spectroscopic samples of Sculptor have the information of colour–magnitudes measured in the Johnson–Morgan system. In order to cross-check our identification, we have used conversion formula of the DES DR1[5] between the DES system and the SDSS system and that of Abbott et al. (2018) and Drlica-Wagner et al. (2018) between the SDSS system and the Jhonson–Morgan system. Then, we have confirmed the consistency between the original magnitudes of the spectroscopic samples and converted magnitudes of the corresponding photometric samples.

[4] Almost all of the spectroscopic star samples can be matched to the photometric samples with a separation angle less than 0.2 arcsec. For each dSph, only a few per cent of the samples are removed from data used in subsequent spectroscopic analyses.

[5] https://des.ncsa.illinois.edu/releases/dr1/dr1-faq

Downloaded from https://academic.oup.com/mnras/article/499/3/3320/5910521 by guest on 23 April 2024

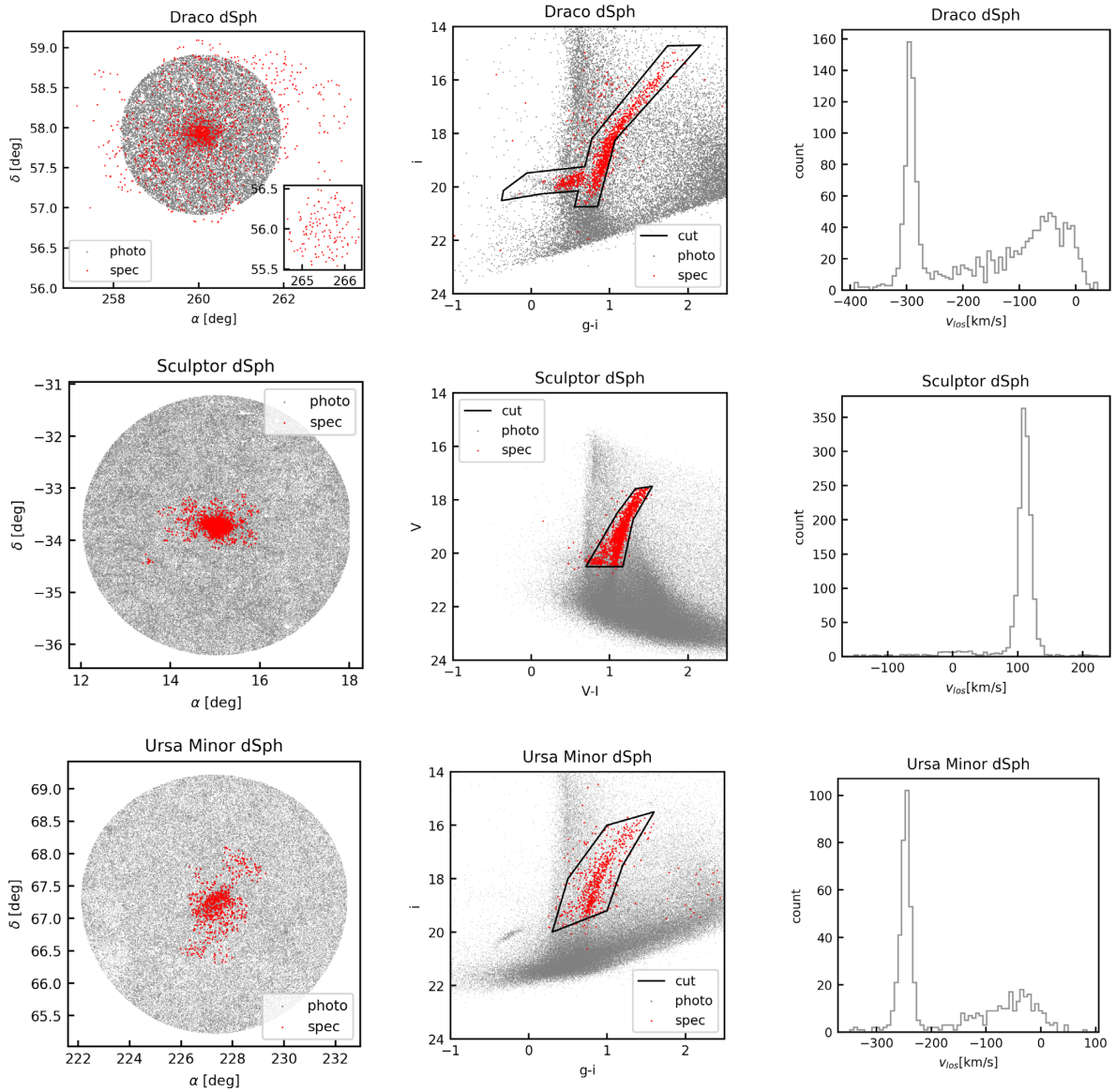

Figure 2. Photometric and spectroscopic samples of Draco (**top row**), Sculptor (**middle row**) and Ursa Minor (**bottom row**). The grey and red dots on scatter plots correspond to the photometric and spectroscopic samples, respectively. **Left column**: Spacial distribution of stars in the equatorial coordinate system. **Centre column**: Colour–magnitude diagram (CMD) with corrections of the reddening. The magnitudes of the spectroscopic samples are obtained from the photometric samples through the catalogue matching. We use the stars in the black polygons for the CMD cut. Note that we use different colour–magnitude systems among the dSphs (SDSS *g* and *i* band for Draco, Johnson *V* and *I* band for Sculptor, Pan-STARRS *g* and *i* band for Ursa Minor, respectively). **Right column**: The histogram of the velocity distribution of the spectroscopic samples we have before the CMD cut (the red points in left and centre columns).

3.3 Colour–magnitude cut

When we estimate membership probabilities of different sample sets such as photometric and spectroscopic ones, we should keep in mind that the membership probability generally depends on the choice of colour–magnitude cuts because the colour–magnitudes of member stars are different from those of foreground stars. In order to guarantee the population of stars to be equal between the photometric and the spectroscopic samples, we impose the same cuts on the colour–magnitude diagram (CMD) in our analysis as shown in Fig. 2. The CMD cut for the Draco dSph is based on that of Walker et al. (2015), which includes red giants and horizontal branch stars. For the Sculptor and Ursa Minor dSphs, we define our cuts with simple polygons including most of the spectroscopic samples.

4 RESULTS

As the result of the stellar density profile selection, the Plummer model is accepted for all the dSphs, though the Bayes factors do not vary much as $\ln \mathrm{BF} \simeq 2 \sim 6$ among the dSphs. It is noteworthy that this selection process will be more important when we consider a stellar model out of more complicated ones because our procedure gives a systematic approach to choose the best one. To confirm the validity of our photometry analysis, we show in Fig. 3 the comparison between the observed surface density and the prediction of the adopted stellar model (obtained by the posterior probability density of the photometry analysis) for each dSph. The grey histograms in the panels of the figure show the binned surface densities of the photometric samples integrated over a ring with a radius R, while the coloured lines shows those obtained by the result of our

Downloaded from https://academic.oup.com/mnras/article/499/3/3320/5910521 by guest on 23 April 2024

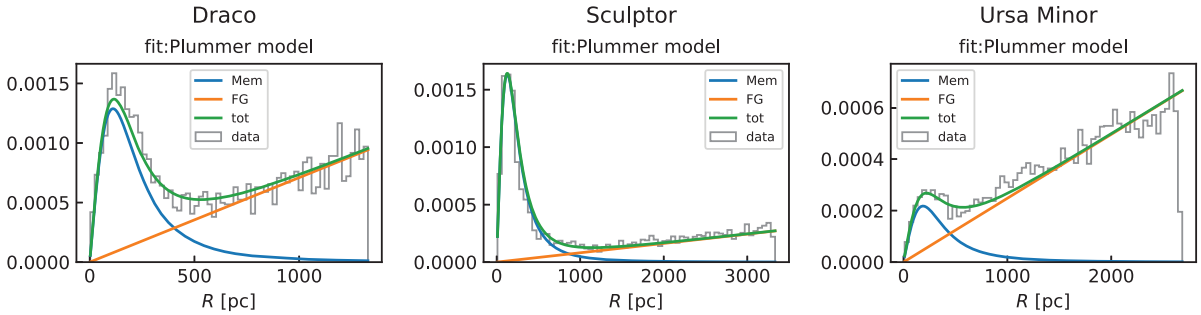

Figure 3. Result of fitting for Draco (**left**), Sculptor (**centre**) and Ursa Minor (**right**) dSphs in the photometric analysis. The grey histograms in the panels show the normalized surface density profile of photometric stars. On the other hand, the coloured lines in the panels show the number density $\Sigma(R)$ times $2\pi R$ of member stars (blue), foreground stars (orange), and all stars (green), respectively, based on the maximum a posteriori (MAP) parameters, which are identical to those obtained by maximum-likelihood estimation because we are using flat priors for the photometric parameters $\Theta_{\rm photo}$ in our analysis.

analysis. Because of a sufficient number of the photometric samples of $\mathcal{O}(10^4)$, their probability density functions (PDFs) converge into Gaussian-like distributions without any prior dependence, which indicates that the result of our photometric analysis with Bayesian statistics is also expected to be achieved even by the analysis with the frequentist statistics. The lines shown in the figure are from estimated number densities computed at the maximum a posteriori parameters, which is nothing but the counterpart of the maximum-likelihood estimation (MLE) or chi-square fittings of the samples in the frequentist statistics.

In the spectroscopic analysis, the WBIC test for the foreground model selection shows that only two foreground components based on the Besançon model are sufficient to fit foreground star distributions of the dSph candidates (Draco, Ursa Minor and Sculptor). This is partially because the foreground stars belonging to the thin disc component have much different colour–magnitude properties from those of the member stars, and thus our cut on the CMD can remove the thin disc stars. Hence, we use the two components model in the spectroscopic analysis.[6]

Posterior PDFs and their correlations are shown in Figs 4, E1 and E2 for Draco, Sculptor and Ursa Minor, respectively. In these figures, for illustration, we convert the velocity dispersion parameters σ_i into $\log_{10}\sigma_i$, odds parameter $\mathrm{Odds}(R_{1/2})$ into $\mathrm{logit}_1 \equiv \ln[\mathrm{Odds}(R_{1/2})]$ and π_i into $\mathrm{logit}_{0,i} \equiv \ln[\pi_i/(1-\pi_i)]$. In Fig. 5, we compare the observed stellar number density in velocity space, denoted by histograms, with those estimated by PDF of spectroscopic analysis, shown by their median values (dashed lines) with their uncertainties (coloured-bands). Similarly, Fig. 6 shows the comparison between observed and estimated velocity dispersion of the member stars, obtained by the PDF of the spectroscopic analysis. Here, blue points with error bars are the observed velocity dispersion calculated by binned samples with the median membership probability $\langle P_M \rangle \geq 0.5$ (member-like stars), while corresponding error bars are obtained by a bootstrap sampling of the stars in the bins. Dashed lines denote the median values of the estimated velocity dispersion, while green and yellow bands are Bayesian credible intervals of 68 per cent and 95 per cent, respectively. We also show maximum a posteriori (MAP) lines by the red line as an analogy of the MLE or simple chi-square fitting.

[6]It is worth notifying that the foreground model selection has the CMD cut dependence as well as the membership probability because each foreground component has its typical magnitudes and velocity distribution. The model selection procedure therefore should be repeated each time in future analyses whenever we use a different sample set with a different CMD cut.

We show our result of J-factor estimation in Table 2 and Fig. 7 as numbers and posterior probability density functions, respectively. Here, the value of the J-factor for each dSph is obtained by integrating the factor within 0.5 deg solid angle, which is nothing but the standard choice of the J-factor estimation (Ackermann et al. 2015). Note also that we take the radius of the outermost star shown in Table 1, which is given by Geringer-Sameth et al. (2015) as a truncation radius of the J-factor estimation to make the estimation the most conservative for the indirect DM detection.[7]

We compare our result to those of other studies in Fig. 8 adopting different methods to treat the contamination effect. The dots and the error bars in the figure denote median values and 68 percent (1σ) Bayesian credible intervals of the posterior probability densities. Our result is shown by the black bars. The red, green, and blue bars show results of Hayashi et al. (2016), Bonnivard et al. (2015), and Geringer-Sameth et al. (2015), respectively, where they adopted the membership selection based on the EM algorithm to remove contaminated stars: Hayashi et al. (2016) considered axisymmetric stellar and DM distributions assuming the generalized NFW profile. In Bonnivard et al. (2015), generalized stellar and DM density distributions are assumed with partially taking the uncertainties of dSph triaxiality into account. Geringer-Sameth et al. (2015) performed similar analysis to ours except the treatment of the contamination effect. The yellow bars are from Ackermann et al. (2015), where the NFW profile is assumed. Authors also assumed a linear relationship among the total luminosity, the maximum circular velocity, and the radius corresponding to the maximum circular velocity, as inferred by Martinez (2015). We summarize these five studies in Table 3.

Finally, Figs 9, E3, and E4 show various correlations between the estimated the J-factor and the model parameters $\Theta_{\rm spec}$ for Draco, Sculptor, and Ursa Minor dSphs, respectively.

5 DISCUSSION

We consider implication of our result presented in the previous section, and discuss the impact of the contamination effect on J-factor estimation. First, we discuss the advantage or our mixture model to estimate proper DM density distributions as well as J-factors of dSphs. Next, we compare our J-factor estimation with those of other studies, and figure out common features among them. Finally, we address characteristics of the J-factor for each dSph.

[7]See Fig. F1 for the impact of the truncation choice on J-factor values.

Downloaded from https://academic.oup.com/mnras/article/499/3/3320/5910521 by guest on 23 April 2024

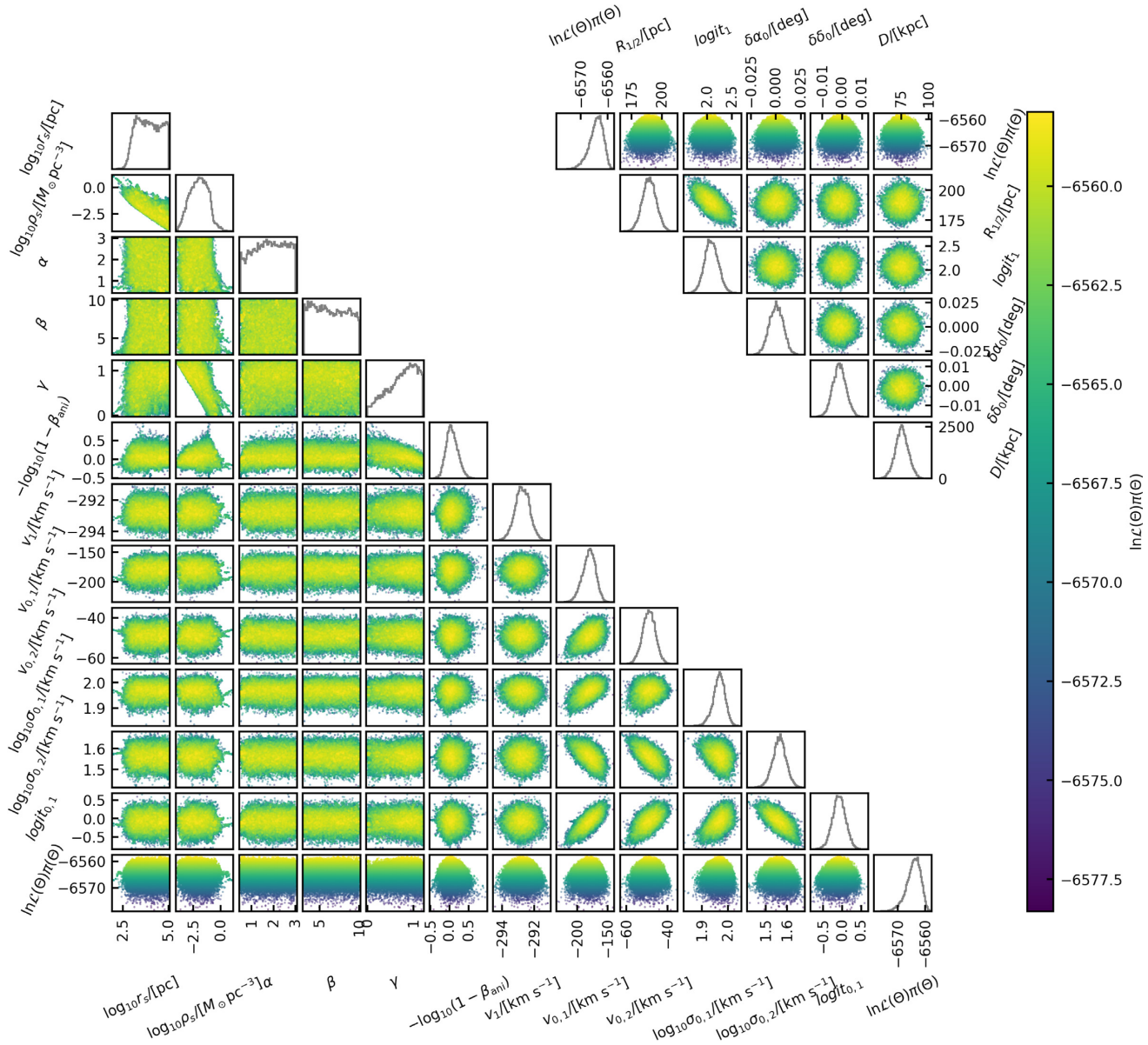

Figure 4. Posterior probability density and correlation matrix for Draco parameters. The upper right triangle corresponds to photometric parameters $\Theta_{\rm photo}$ as well as a spectroscopic parameter D, while the lower left triangle corresponds to the spectroscopic ones $\Theta_{\rm spec}$ except D. For illustration, we convert the velocity dispersion parameters σ_i into $\log_{10}\sigma_i$, odds parameter $\mathrm{Odds}(R_{1/2})$ into $\mathrm{logit}_1 \equiv \ln(\mathrm{Odds}(R_{1/2}))$ and π_i into $\mathrm{logit}_{0,i} \equiv \ln(\pi_i/(1-\pi_i))$.

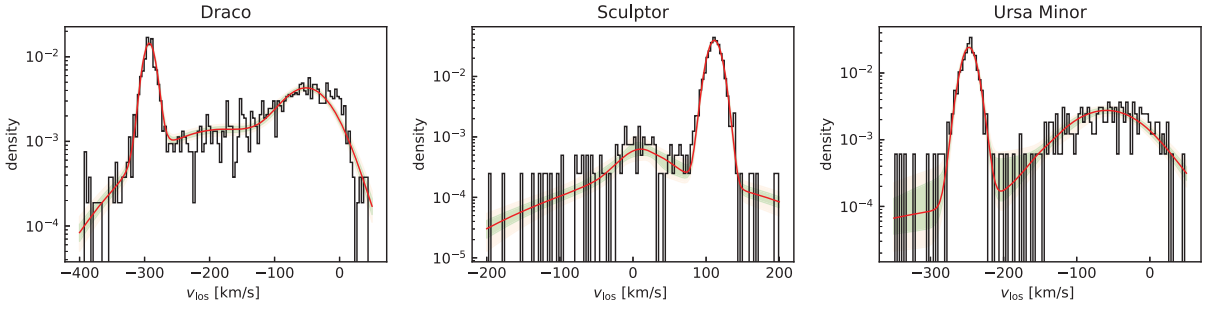

Figure 5. Comparison between observed and estimated velocity distribution of stars for Draco (**left**), Sculptor (**centre**), and Ursa Minor (**right**). The grey histograms are binned number density of observed stars in velocity space. Bayesian credible intervals of 68 per cent and 95 per cent are shown by the green and yellow bands. Maximum a posteriori (MAP) lines are also shown by the red lines.

Downloaded from https://academic.oup.com/mnras/article/499/3/3320/5910521 by guest on 23 April 2024

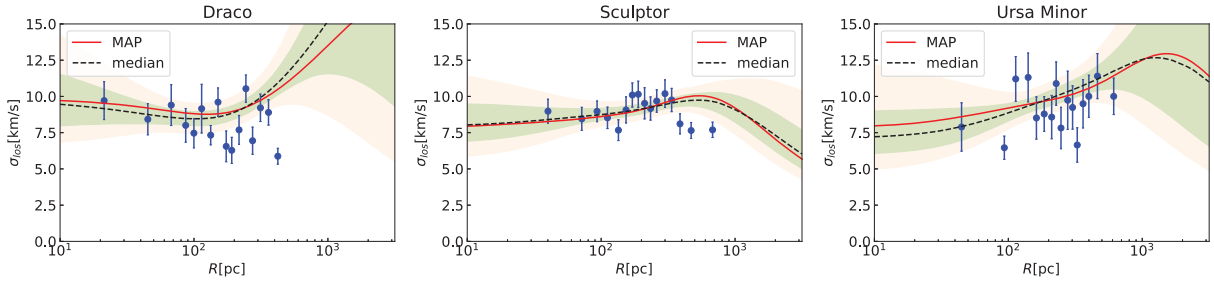

Figure 6. Comparison between observed and estimated velocity dispersion of the member stars for Draco (**left**), Sculptor (**centre**), and Ursa Minor (**right**). The blue points are observed dispersion with error bars obtained by a bootstrap sampling. The dashed lines denote the median values of the estimated dispersion associated with Bayesian credible intervals of 68 per cent and 95 per cent shown by the green and yellow bands. MAP lines are also shown by the red lines.

Table 2. Result of *J*-factor estimation. The median value of the posterior probability density function is shown for each dSph. Lower and upper errors correspond to the 1σ range of the PDF (16th and 84th percentiles).

dSph	ν, Σ	$\log_{10}(J(0.5^\circ)/[\mathrm{GeV^2cm^{-5}}])$
Draco	Plummer	$18.96^{+0.21}_{-0.17}$
Sculptor	Plummer	$18.53^{+0.12}_{-0.11}$
Ursa Minor	Plummer	$18.75^{+0.17}_{-0.13}$

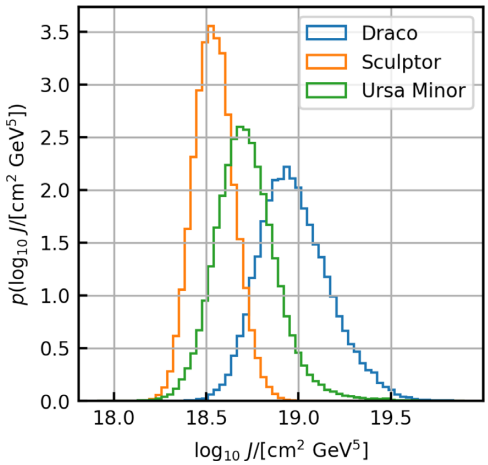

Figure 7. The posterior density function (PDF) of the *J*-factor for each dSph, obtained by the MCMC calculation. The blue, orange, and green lines correspond to the PDFs for Draco, Sculptor, and Ursa Minor, respectively. Here, the vertical axis is normalized to satisfy $\int \mathrm{d}(\log_{10}J)p(\log_{10}J) = 1$.

5.1 Common features

The result in Fig. 6 suggests the importance of properly taking an uncertainty from membership probability into account. It shows that line-of-sight velocity dispersion predicted by our method has a large uncertainty at the outer region, where the most observed stars are indeed from foreground stars. In terms of the Bayesian statistical estimation, data points at the region have more importance than those at regions with many data points. In the conventional analysis, many foreground stars at the outer region are likely to be misidentified as 'member' stars even if we impose a rigorous membership selection. Hence, parameter estimation based on the membership selection is often affected by the contamination effect, and it induces an additional systematical uncertainty. In contrast, the mixture model can deal with this uncertainty by the statistical analysis in a straightforward way because the model includes the contamination effect in the definition of the likelihood function.

On the other hand, Figs 9, E3, and E4 show that estimated *J*-factors are correlated with the distance parameter *D*. The correlation between the *J*-factor and the distance *D* is fitted by the linear regression, $\log_{10}(J/\mathrm{GeV^2cm^{-5}}) = a\log_{10}(D/\mathrm{pc}) + b$, with regression coefficients being $a = -3.23$ and $b = 34.73$. As discussed in Appendix C, the coefficient a takes a value of $a \sim 3$, where the small difference from the exact expectation ($a = 3$) comes from other uncertainties such as the contamination effect. Indeed, the coefficient is closer to the expected value for the Sculptor case ($a = -2.93$) due to a lower contamination ($\mathrm{logit}_1 \sim 4.2$ or $s_{R_{1/2}} \sim 0.99$). The uncertainty of the distance between dSph and Solar system causes a non-negligible uncertainty on *J*-factor estimation, especially for the case of dSph with low contamination such as Sculptor.

Figs 9, E3, and E4 also show that the *J*-factor can be correlated with the DM profile parameter γ (inner slope). It indicates that the analysis adopting the generalized NFW profile (or some other analyses that allow the DM profile having an enough freedom to change the inner slope) is important rather than analyses with the profile having a fixed inner slope from the first beginning.

Fig. 8 shows that *J*-factors obtained in our analysis are more or less consistent with those obtained by other studies, however, their means and errors are slightly different from our result. These differences can be used to discuss validity of assumptions made in each study. For instance, the error bars of Hayashi et al. (2016) are larger than other studies, and it suggests that the uncertainty from the axisymmetricity of dSph is underestimated by assuming the sphericity of dSph. Indeed, (log-)Bayes factors complied by Hayashi et al. (2016) take large values (>10), which is larger than those obtained by analyses assuming the sphericity.

5.2 Draco

The value of the J-factor for the Draco dSph reported by Geringer-Sameth et al. (2015) is slightly smaller than ours, and it must be from the contamination effect because their analysis is almost the same as ours except the treatment of the contamination (and some prior set-ups). Indeed, in contrast with the fact that our 'member' stars in Fig. 6 are located within $R \lesssim 500$ pc, their 'member' stars shown in fig. 1 of Geringer-Sameth et al. (2015) are distributed as far as $R \sim 1000$ pc. The stars and their velocity dispersion with a somewhat suppressed value at the outer region are expected to be from the flatting bias of their EM algorithm. This suppressed dispersion profile is then

Downloaded from https://academic.oup.com/mnras/article/499/3/3320/5910521 by guest on 23 April 2024

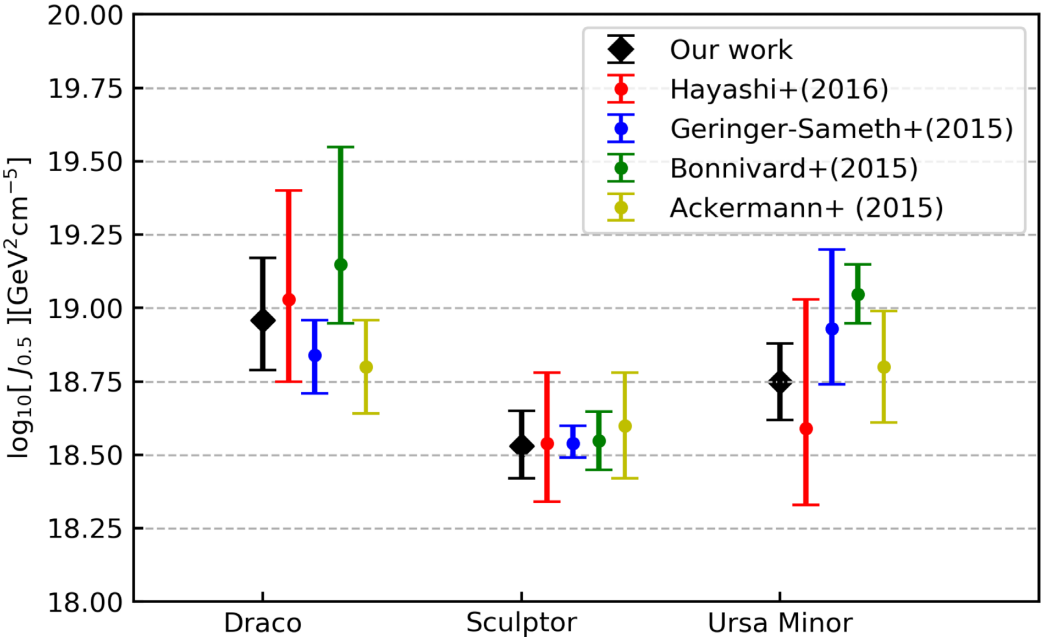

Figure 8. Comparison among various *J*-factor estimations. Our result is shown by the black dots error bars. We also show results estimated by other studies (Ackermann et al. 2015; Bonnivard et al. 2015; Geringer-Sameth et al. 2015) with the blue, green, and yellow ones, respectively. For the red ones, we present our (previous) result obtained by performing a more generalized fitting (adopting the generalized NFW profile) than the original one in Hayashi et al. (2016).

Table 3. Comparison of analysis methods in Fig. 8. Note that the stellar and anisotropy models of Ackermann et al. (2015) are not specified in the table because they adopt the Bayesian hierarchical modelling, where the Jeans equation appears as an integrated form without explicit dependence on stellar and anisotropy models. We also note that Bonnivard et al. (2015) takes the uncertainty coming from the triaxiality into account to estimate *J*-factor uncertainties.

Work	Symmetry	ν_1, Σ_1	$\rho_{\rm DM}$	$\beta_{\rm ani}$	FG contami.
Our study	Spherical	Plummer/exp.	Generalized NFW	Constant	Mixture model
Hayashi et al. (2016)	Axisymmetric	Plummer	Generalized NFW	Constant	P_M cut
Geringer-Sameth et al. (2015)	Spherical	Plummer	Generalized NFW	Constant	P_M cut
Bonnivard et al. (2015)	Spherical (triaxial)	Generalized NFW	Generalized Einasto	Baes & Van Hese (2007)	P_M cut
Ackermann et al. (2015)	Spherical	-	NFW	-	Hierarchical modelling

fitted by a more radial anisotropy.[8] The suppressed profile, on the other hand, also requires a more concentrated DM profile (smaller $r_{\rm s}$ with $\rho(r)$ being enough large at the inner region). As a result, the *J*-factor in their analysis is predicted to be smaller than what we have obtained. Geringer-Sameth et al. (2015) reported less *J*-factor error than ours, and this is partially because they utilize information of metallicity for the stellar membership calculation.

5.3 Sculptor

The value of the *J*-factor for Sculptor dSph is not sizeably different from each other. This is because the contamination rate of the Sculptor is quite small as mentioned in Section 5.1, and the P_M cut procedure works very well. Fig. 8 also shows that the error bar of Geringer-Sameth et al. (2015) is smaller than ours, which is partially because they imposed additional kinematical and cosmological constraints on DM profiles, namely, the criteria on truncation radius and central density. It is also worth notifying that the *J*-factor of Sculptor is significantly dependent on its distance to the Solar system due to the low contamination uncertainty, as mentioned in Section 5.1. This strong correlation suggests that the major uncertainty of the *J*-factor is from the uncertainty of the distance *D*, and it means that further study of the distance determination is required to obtain a more precise *J*-factor for the Sculptor dSphs.

5.4 Ursa Minor

In contrast to the Draco case, Geringer-Sameth et al. (2015) obtained a slightly larger value of the *J*-factor than ours.[9] This fact is expected to be from the contamination as in the case of the Draco, though it affects the dispersion profile in a different way. Our dispersion profile has its maximum at $R \simeq 1000$ pc, while the maximum of their profile is at $R \simeq 200$ pc. The maximum at smaller *R* in their analysis requires more compact DM profile (smaller $r_{\rm s}$ and larger $\rho_{\rm s}$) than ours. On the other hand, the compact DM profile also induces the increase of the profile at inner region, and it must be compensated by more tangential anisotropy.[10] As a result, the *J*-factor value of Geringer-Sameth et al.

[8]Geringer-Sameth et al. (2015) reported $-\log_{10}(1-\beta_{\rm ani}) = 0.54^{+0.27}_{-0.29}$, while our result is more isotropic, $-\log_{10}(1-\beta_{\rm ani}) = 0.06^{+0.16}_{-0.14}$.

[9]Bonnivard et al. (2015) also obtained a significantly larger *J*-factor than ours. This is because that they adopted a larger truncation radius than the outermost radius, which is motivated from the tidal radius of the Ursa Minor.

[10]Indeed, Geringer-Sameth et al. (2015) obtained tangential anisotropy, $-\log_{10}(1-\beta_{\rm ani}) = -0.47^{+0.28}_{-0.32}$, and compact DM profile,

Downloaded from https://academic.oup.com/mnras/article/499/3/3320/5910521 by guest on 23 April 2024

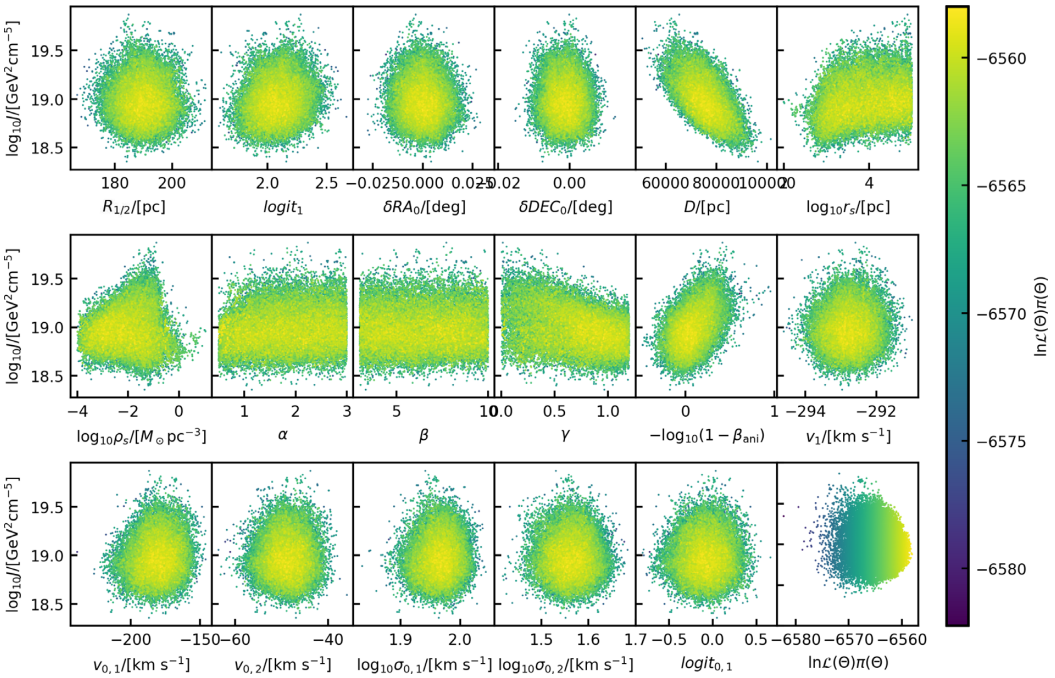

Figure 9. Correlation between the *J*-factor PDF and various model parameters for Draco dSph.

(2015) becomes larger than our result. Here, it is worth notifying that the compact DM profile contributes to the *J*-factor values conversely compared to the Draco case. This difference comes from the fact that the flattened dispersion profile of the Draco requires the compact DM profile and radial anisotropy, while that of the Sculptor requires the compact DM profile and tangential anisotropy. Moreover, we obtained less *J*-factor error than what Geringer-Sameth et al. (2015) reported, and this is partially because our estimate of r_s is larger than the truncation radius of the *J*-factor, so that the uncertainty of the DM profile does not contribute the *J*-factor uncertainty so much.

6 CONCLUSIONS

We have estimated the *J*-factors of Draco, Sculptor, and Ursa Minor dSphs, which are known to be promising targets for the indirect DM detection utilizing various gamma-ray observations. We have adopted a mixture model for member and foreground star distributions based on a conditional likelihood function for a given projected distance from the dSph centre, which is obtained by improving the likelihood function proposed in KI and useful to remove sampling bias that we often suffer in spectroscopic observation.

We introduced a new parameter Odds($R_{1/2}$) concerning the membership ratio, which allows us to have a well-determined prior function of the parameter from photometric observation. *J*-factors obtained in our analysis are consistent with those of previous studies, but we saw some small differences among the studies at the same time, which is in particular apparent for higher contaminated dSphs such as Draco and Ursa Minor. Moreover, we found that the uncertainty of the distance measurement gives a sizeable uncertainty on *J*-factor estimation in some cases. It is thus important to determine the distance accurately to estimate *J*-factor precisely.

Spectroscopic observation with a large field of view in the near future such as the PFS will enable us to observe thousands of stars simultaneously and to estimate *J*-factors for various dSphs more precisely. Proper treatment of the foreground contamination hence becomes more and more important, for the number of contaminated foreground stars increases in the data set. In particular, we can expect that the method developed in this paper will be a powerful tool to estimate *J*-factors of ultrafaints dSphs in near future, as they suffer the contamination more seriously.

ACKNOWLEDGEMENTS

We would like to give special thanks to Koji Ichikawa for his recent researches, as well as the kindness to give us his old computational resources. This research has used ASTROPY,[11] a community-developed core PYTHON package for Astronomy (Robitaille et al. 2013; Price-Whelan et al. 2018). This work was supported by JSPS KAKENHI Grant Numbers, 18H04359 & 18J00277 for KH, 15H05889 & 16H03991 & 18H05542 for MI, 17K14249 for MNI, 19H05810 & 16H02176 for SM, 17H02878 for MI & SM, and 18J21186 for SH. Finally, Kavli IPMU is supported by World Premier International Research Centre Initiative (WPI), MEXT, Japan.

DATA AVAILABILITY

The data underlying this article will be shared on reasonable request to the corresponding author.

REFERENCES

Abbott T. M. C. et al., 2018, ApJS, 239, 18
Abolfathi B. et al., 2018, ApJS, 235, 42

$\log_{10}(\rho_s/M_\odot\ \mathrm{pc}^3) = -0.50^{+0.60}_{-0.64}$ & $\log_{10}(r_s/\mathrm{pc}) = 2.60^{+0.40}_{-0.38}$, while we obtained less tangential anisotropy, $-\log_{10}(1-\beta_{\mathrm{ani}}) = -0.20^{+0.18}_{-0.24}$, and more diluted DM profile, $\log_{10}(\rho_s/M_\odot\ \mathrm{pc}^3) = -1.55^{+0.69}_{-1.07}$ & $\log_{10}(r_s/\mathrm{pc}) = 3.42^{+0.91}_{-0.50}$.

[11] http://www.astropy.org

Downloaded from https://academic.oup.com/mnras/article/499/3/3320/5910521 by guest on 23 April 2024

Ackermann M. et al., 2015, Phys. Rev. Lett., 115, 231301
Ade P. A. R., others, 2016, A&A, 594, A13
Alvarez A., Calore F., Genina A., Read J. I., Serpico P. D., Zaldivar B., 2020, J. Cosmol. Astropart. Phys., 2020, 004
Baes M., Van Hese E., 2007, A&A, 471, 419
Battaglia G., Helmi A., Tolstoy E., Irwin M., Hill V., Jablonka P., 2008, ApJ, 681, L13
Bhattacherjee B., Ibe M., Ichikawa K., Matsumoto S., Nishiyama K., 2014, J. High Energy Phys., 2014, 80
Binney J., Tremaine S., 2008, Galactic Dynamics, 2nd. Princeton Univ. Press, Princeton, NJ
Bonnivard V. et al., 2015, MNRAS, 453, 849
Bonnivard V., Maurin D., Walker M. G., 2016, MNRAS, 462, 223
Bradac M. et al., 2006, ApJ, 652, 937
Burkert A., 1995, ApJ, 447, 10
Chambers K. C. et al., 2016, preprint (arXiv:1612.05560)
Cholis I., Salucci P., 2012, Phys. Rev. D, 86, 023528
Clowe D., Bradac M., Gonzalez A. H., Markevitch M., Randall S. W., Jones C., Zaritsky D., 2006, ApJ, 648, L109
Coleman M. G., Da Costa G. S., Bland-Hawthorn J., 2005, AJ, 130, 1065
Dehnen W., 1993, MNRAS, 265, 250
Drlica-Wagner A. et al., 2018, ApJS, 235, 33
Evans J. L., Ibe M., Olive K. A., Yanagida T. T., 2013, Eur. Phys. J. C, 73, 2468
Foreman-Mackey D., Hogg D. W., Lang D., Goodman J., 2013, PASP, 125, 306
Geringer-Sameth A., Koushiappas S. M., Walker M., 2015, ApJ, 801, 74
Hastings W. K., 1970, Biometrika, 57, 97
Hayashi K., Ichikawa K., Matsumoto S., Ibe M., Ishigaki M. N., Sugai H., 2016, MNRAS, 461, 2914
Hernquist L., 1990, ApJ, 356, 359
Hisano J., Matsumoto S., Nagai M., Saito O., Senami M., 2007, Phys. Lett., B646, 34
Ichikawa K., Ishigaki M. N., Matsumoto S., Ibe M., Sugai H., Hayashi K., Horigome S., 2017, MNRAS, 468, 2884
Ichikawa K., Horigome S., Ishigaki M. N., Matsumoto S., Ibe M., Sugai H., Hayashi K., 2018, MNRAS, 479, 64
Irwin M., Hatzidimitriou D., 1995, MNRAS, 277, 1354
Jasra A., Holmes C. C., Stephens D. A., 2005, Stat. Sci., 20, 50
Koch A., Kleyna J. T., Wilkinson M. I., Grebel E. K., Gilmore G. F., Evans N. W., Wyse R. F. G., Harbeck D. R., 2007, AJ, 134, 566
Lefranc V., Moulin E., Panci P., Sala F., Silk J., 2016, J. Cosmol. Astropart. Phys., 2016, 043
Martin N. F., de Jong J. T. A., Rix H.-W., 2008, ApJ, 684, 1075
Martinez G. D., 2015, MNRAS, 451, 2524
Martinez G. D., Bullock J. S., Kaplinghat M., Strigari L. E., Trotta R., 2009, J. Cosmol. Astropart. Phys., 0906, 14
Martinez G. D., Minor Q. E., Bullock J., Kaplinghat M., Simon J. D., Geha M., 2011, ApJ, 738, 55
Mateo M., Olszewski E. W., Walker M. G., 2008, ApJ, 675, 201
McConnachie A. W., 2012, AJ, 144, 4
McLaughlin D. E., 1999, ApJ, 512, L9
Metropolis N., Rosenbluth A. W., Rosenbluth M. N., Teller A. H., Teller E., 1953, J. Chem. Phys., 21, 1087
Moroi T., Randall L., 2000, Nucl. Phys. B, 570, 455
Navarro J. F., Frenk C. S., White S. D. M., 1997, ApJ, 490, 493
Pace A. B. et al., 2020, MNRAS, 495, 3022
Plummer H. C. C., 1911, MNRAS, 71, 460
Price-Whelan A. M. et al., 2018, AJ, 156, 123
Read J. I., Steger P., 2017, MNRAS, 471, 4541
Read J. I., Walker M. G., Steger P., 2018, MNRAS, 481, 860
Robin A. C., Reyle C., Derriere S., Picaud S., Reylé C., Derrière S., Picaud S., 2003, A&A, 409, 523
Robitaille T. P. et al., 2013, A&A, 558, A33
Rubin V. C. C., Thonnard N., Ford W. K. J., 1978, ApJ, 225, L107
Rubin V. C., Ford W. K. J., Thonnard N., 1980, ApJ, 238, 471
Schwarz G., 1978, Ann. Stat., 6, 461
Ségall M., Ibata R. A., Irwin M. J., Martin N. F., Chapman S., 2007, MNRAS, 375, 831
Simon J. D., Geha M., 2007, ApJ, 670, 313
Spencer M. E., Mateo M., Olszewski E. W., Walker M. G., McConnachie A. W., Kirby E. N., 2018, AJ, 156, 257
Sugai H. et al., 2015, J. Astron. Telesc. Instrum. Syst., 1, 035001
Takada M. et al., 2014, PASJ, 66, R1
Tamura N. et al., 2016, in Evans C. J., Simard L., Takami H., eds, Proc. SPIE Conf. Ser. Vol. 9908, Ground-based and Airborne Instrumentation for Astronomy VI . SPIE, Bellingham, p. 9081M
Tolstoy E. et al., 2004, ApJ, 617, L119
Ullio P., Valli M., 2016, J. Cosmol. Astropart. Phys., 2016, 025
Walker M. G., Mateo M., Olszewski E. W., 2009a, AJ, 137, 3100
Walker M. G., Mateo M., Olszewski E. W., Sen B., Woodroofe M., 2009b, AJ, 137, 3109
Walker M. G., Olszewski E. W., Mateo M., 2015, MNRAS, 448, 2717
Watanabe S., 2012, J. Mach. Learn. Res., 14, 867
Zhao H., 1996, MNRAS, 278, 488
Zwicky F., 1933, Helv. Phys. Acta, 6, 110

Downloaded from https://academic.oup.com/mnras/article/499/3/3320/5910521 by guest on 23 April 2024

Table A1. Probabilities and probability density functions used in our likelihood function. Note that we always put random variables on the left-hand-side of the bracket, (|), while conditions are put on the right-hand side.

Notation	Description
$p(v, R)$	Simultaneous probability to find a star at the radius R and at the velocity v.
$p(v, R\|M)$	The same as above but for member stars ($M = 1$) and foreground stars ($M = 0$).
$p(R\|M)$	Normalized stellar density profile for member and foreground stars ($\int \mathrm{d}R p(R\|M) = 1$).
$p(M\|R)$	Local membership probability at radius R.
$p(M)$	Global membership probability. It depends on the CMD cut criteria and RoI selections.

APPENDIX A: IMPROVING KI17 LIKELIHOOD

We derive our likelihood function from that of KI based on the assumptions made in Section 2. [12] Here, the likelihood function $\mathcal{L}$ for the spectroscopic data is defined as follows:

$$\mathcal{L}_{\rm KI17} = \prod_i [s f_1(v_i, R_i) + (1-s) f_0(v_i, R_i)] \,. \tag{A1}$$

This is based on the PDF $p(\boldsymbol{v}, \boldsymbol{R}) \equiv \prod_i \sum_{M_i=1,0} p(M_i) p(v_i, R_i|M_i)$, where $p(M=1) = s$ and $p(v, R|M) = f_M(v, R)$.[13] In order to obtain a likelihood that is free from sampling bias, we use the conditional probability $p(\boldsymbol{v}|\boldsymbol{R})$ instead of $p(\boldsymbol{v}, \boldsymbol{R})$ as a new likelihood function as follows:

$$\mathcal{L}_{\rm spec} \equiv p(\boldsymbol{v}|\boldsymbol{R}), \tag{A2}$$

$$= \prod_i \sum_{M_i} p(M = M_i|R_i) p(v_i|R_i, M_i), \tag{A3}$$

$$\equiv \prod_i [s(R_i)\mathcal{G}_1(v_i) + [1 - s(R_i)]\mathcal{G}_0(v_i)] \,, \tag{A4}$$

where the local membership probability $s(R)$ is given by the formula

$$s(R) \equiv p(M=1|R) = \frac{p(M=1)\int \mathrm{d}v p(v, R|M=1)}{\sum_M p(M)\int \mathrm{d}v p(v, R|M)}, \tag{A5}$$

$$= [1 + (\frac{s\int \mathrm{d}v f_1(v, R)}{(1-s)\int \mathrm{d}v f_0(v, R)})^{-1}]^{-1}. \tag{A6}$$

Here, it is worth pointing out that the integral $\int \mathrm{d}v f_M(v, R)$ are proportional to the projected stellar density function $\Sigma_M(R)$ when $\int \mathrm{d}v = \int_{-\infty}^{\infty} \mathrm{d}v$, because we assume that the distribution function $f_M(v, R)$ has the velocity dependence only through the Gaussian function, whose integral is given by $\int_{-\infty}^{\infty} \mathrm{d}v \mathcal{G}(v; v_M, \sigma_M(R)) = 1$.[14] In this case, s_R is simplified as follows:

$$s(R) = [1 + \frac{1}{\mathrm{Odds}(R_{1/2})} \frac{\Sigma_1(R_{1/2})/\Sigma_1(R)}{\Sigma_0(R_{1/2})/\Sigma_0(R)}]^{-1} \,, \tag{A7}$$

where the ratio $\Sigma_0(R)/\Sigma_0(R_{1/2})$ is always one in our analysis because we have assumed uniform stellar density for foreground stars. Then, the local odds $\mathrm{Odds}(R_{1/2})$ is given as follows:

$$\mathrm{Odds}(R_{1/2}) \equiv \frac{p(M=1|R=R_{1/2})}{p(M=0|R=R_{1/2})} \tag{A8}$$

$$= \frac{s}{1-s} \frac{\int \mathrm{d}v f_1(v, R_{1/2})}{\int \mathrm{d}v f_0(v, R_{1/2})} \,. \tag{A9}$$

Hence, we adopt $\mathrm{Odds}(R_{1/2})$ as an alternative parameter of s. The advantage of this parametrization is that we can define the membership probability of a specific dSph without sampling bias, allowing us to utilize several data sets from different observations, for example, the photometry data and the spectroscopy data in this work.[15]

APPENDIX B: GENERALIZED LIKELIHOOD

We discuss the validity of our assumptions (iv) and (v) in Section 2 using a generalized likelihood function, which is defined by

$$\mathcal{L}_{\rm gen} \equiv \prod_i \sum_{M_i} p(v_i, R_i, M_i, \boldsymbol{Z}_i), \tag{B1}$$

where $\boldsymbol{Z}_i \equiv W_i, C_i, \cdots$ denotes additional observable such as metallicity W_i, colour–magnitude C_i, etc. Our likelihood function equation (A3) and (11) is derived by: 1. conditionalizing this likelihood function by position R_i, and 2. marginalizing it over $\boldsymbol{Z}$ space;

$$\mathcal{L}_{\rm spec} \equiv \prod_i \frac{\int \mathrm{d}\boldsymbol{Z}_i \mathcal{L}_{\rm gen}}{\int \mathrm{d}v_i \int \mathrm{d}\boldsymbol{Z}_i \mathcal{L}_{\rm gen}}, \tag{B2}$$

$$= \prod_i \sum_{M_i} \int \mathrm{d}\boldsymbol{Z}_i \, p(v_i|R_i, M_i, \boldsymbol{Z}_i) p(M_i|R_i, \boldsymbol{Z}_i) p(\boldsymbol{Z}_i|R_i) \,, \tag{B3}$$

$$= \prod_i \sum_{M_i} p(v_i|R_i, M_i) p(M_i|R_i) \,, \tag{B4}$$

where

$$p(M_i|R_i) = \int \mathrm{d}\boldsymbol{Z}_i \, p(M_i|R_i, \boldsymbol{Z}_i) p(\boldsymbol{Z}_i|R_i), \tag{B5}$$

$$p(v_i|R_i, M_i) = \int \mathrm{d}\boldsymbol{Z}_i \, p(v_i|R_i, M_i, \boldsymbol{Z}_i) \frac{p(M_i|R_i, \boldsymbol{Z}_i) p(\boldsymbol{Z}_i|R_i)}{p(M_i|R_i)} \,. \tag{B6}$$

Our assumption (v) (colour–magnitude independence of the member distribution) corresponds to

$$p(v_i, \boldsymbol{Z}_i|R_i, M_i = 1) = p(v_i|R_i, M_i = 1) p(\boldsymbol{Z}_i|R_i, M_i = 1) \,, \tag{B7}$$

which is equivalently written by

$$p(v_i|R_i, M_i = 1, \boldsymbol{Z}_i) = p(v_i|R_i, M_i = 1) \,. \tag{B8}$$

Based on this assumption, we have constructed a concrete likelihood function, as shown in the main text. For the verification of this assumption, we have checked the goodness of fit of our spectroscopic estimation by computing $\chi^2 \equiv \sum_i (v_i - v_1)^2/\sigma^2(R_i)$ for member-like stars. As a result, obtained minimum χ^2 values satisfy $\chi^2 \simeq O(N_1)$, where N_1 denotes the number of member stars, which validate this assumption for present data sets.

It has been reported that Sculptor and Ursa Minor have colour–magnitude dependent stellar kinematics (Tolstoy et al. 2004; Battaglia et al. 2008; Pace et al. 2020). Further analysis including such dependencies might help us to obtain more accurate DM distribution, especially when larger spectroscopic data sets are available in future.

[12] The validity of the assumptions are discussed in Appendix B.
[13] We summarize definitions of the probabilities in Table A1.
[14] In the case of the finite-ranged integration, $\int \mathrm{d}v f_M(v, R)$ gives another R-dependent factor, which comes from $\int \mathrm{d}v \mathcal{G}(v; v_M, \sigma_M(R))$.
[15] Moreover, the use of s causes another trouble: when we observe all stars from the dSph centre to the radius R that is much away from the centre, s becomes almost 0 because the number of member stars are finite at $R \to \infty$, while that of contaminating foreground stars is proportional to R^2.

Downloaded from https://academic.oup.com/mnras/article/499/3/3320/5910521 by guest on 23 April 2024

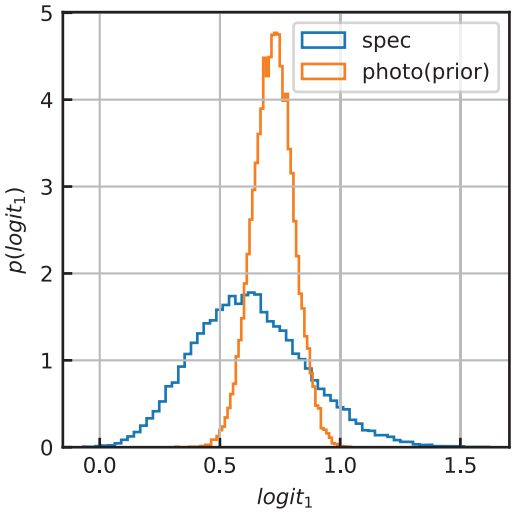

Figure B1. Comparison of the posterior distribution of the membership probability, Odds($R_{1/2}$), of the photometric analysis with that of the spectroscopic analysis without using the photometric posterior distribution as a prior distribution in the case of Ursa Minor. The horizontal axis represents $\mathrm{logit}_1 \equiv \ln(\mathrm{Odds}(R_{1/2}))$. The orange correspond to the prior distribution, while the blue one denotes the posterior distribution.

The assumption (iv; randomness of spectroscopic samples) assumes that the photometric and the spectroscopic samples have the same probability distribution $p(v_i, R_i, M_i, \mathbf{Z_i})$ in equation (B1). If the spectroscopic samples are biased in colour–magnitude space, it affects the membership probability through the $\mathbf{Z_i}$ integration in equation (B5). To validate the assumption (iv), we compare the posterior distribution of the membership probability, Odds($R_{1/2}$), of the photometric analysis with that of the spectroscopic analysis without using the photometric posterior distribution as a prior distribution. We show the comparison in Fig. B1 in the case of Ursa Minor as an example. Here, the orange line correspond to the prior distribution, while the blue one denotes the posterior distribution obtained from the spectroscopic analysis without the prior. It can be seen that the prior distribution from the photometric analysis is well contained in the posterior distribution.

APPENDIX C: DISTANCE DEPENDENCE OF J-FACTOR

J-factor depends strongly on the distance to a dSph. Ullio & Valli (2016) shows that, for a given distance D, a spherical dSph with the DM density profile $\rho_{\rm DM}(r)$ has the following dependence:

$$J_D \simeq \frac{4\pi}{D^2}\int_0^{r_{\rm max}} {\rm d}r r^2 \rho_{\rm DM}^2(r)\,. \tag{C1}$$

The DM density profile $\rho_{\rm DM}(r)$ also depends implicitly on D due to the invariance of the observed line-of-sight velocity dispersion $\sigma^2_\Theta(R)$ (Θ: parameters). Namely, for a distance $D^{'} = kD$, a observed radius of a star R is also scaled by the factor k because of $R = D\sin\theta$, and the re-scaled line-of-sight velocity dispersion $\sigma^2_{\Theta'}(R')$ with different parameters $\Theta^{'} \ni D^{'}$ and a radius $R^{'} = kR$ must be equal to the original one as $\sigma^2_\Theta(R) = \sigma^2_{\Theta'}(R')$. Here,

$$\Theta = \rho_{\rm s},\ r_{\rm s},\ R_{1/2},\ D\,, \tag{C2}$$

$$\Theta' = \rho'_{\rm s},\ r'_{\rm s},\ R'_{1/2},\ D' = k^{-2}\rho_{\rm s},\ kr_{\rm s},\ kR_{1/2},\ kD\,. \tag{C3}$$

This relationship can be confirmed as follows: The stellar number densities and the DM density profile are in general defined as

$$\Sigma_1(R) = R_{\rm e}^{-2} f_1(R/R_{\rm e})\,, \tag{C4}$$

$$\nu_1(r) = R_{\rm e}^{-3} f_2(r/R_{\rm e})\,, \tag{C5}$$

$$\rho_{\rm DM}(r) = \rho_{\rm s} f_3(r/r_{\rm s})\,, \tag{C6}$$

$$M(r) = \rho_{\rm s} r_{\rm s}^3 f_4(r/r_{\rm s})\,. \tag{C7}$$

Substituting them into equations (8) and (9) leads to

$$\sigma^2_{\Theta'}(R') = \frac{2}{k^{-2}\Sigma_1(R)}\int_{kR}^{\infty}\frac{{\rm d}r}{\sqrt{1-(kR)^2/r^2}}\left(1-\beta_{\rm ani}\frac{(kR)^2}{r^2}\right) \times \int_r^{\infty} k^{-3}\nu_1(r')\left(\frac{r'}{r}\right)^{2\beta_{\rm ani}}\frac{k^{-2+3}GM(r')}{r'^2}{\rm d}r', \tag{C8}$$

$$= \frac{2}{k^{-2}\Sigma_1(R)}\int_{R}^{\infty}\frac{k{\rm d}r}{\sqrt{1-R^2/r^2}}\left(1-\beta_{\rm ani}\frac{R^2}{r^2}\right) \times \int_r^{\infty} k^{-3}\nu_1(r')\left(\frac{r'}{r}\right)^{2\beta_{\rm ani}}\frac{k^{-2+3}GM(r')}{k^2 r'^2}k{\rm d}r' \tag{C9}$$

$$= \sigma^2_\Theta(R)\,. \tag{C10}$$

It means that our likelihood function has a degeneracy, and we obtain the J-factor for a different input distance $D^{'} = kD$ as

$$J_{D'} \simeq \frac{4\pi}{k^2 D^2}\int_0^{kr_{\rm max}} {\rm d}r r^2 \rho^2_{\rm DM}(kr)|_{r_{\rm s}=kr_{\rm s}}\,, \tag{C11}$$

$$= \frac{4\pi}{k^2 D^2}\int_0^{r_{\rm max}} k{\rm d}r k^2 r^2 k^{-2\times 2}\rho^2_{\rm DM}(r) = k^{-3} J_D\,. \tag{C12}$$

As a result, estimation on the J-factor is non-negligibly affected by the uncertainty of the distances D. For instance, 10 per cent error of the distance $k = 1.0^{+0.1}_{-0.1}$ gives $\log_{10} J'_D = (\log_{10} J_D)^{+0.12}_{-0.14}$.

APPENDIX D: WIDELY APPLICABLE BAYESIAN INFORMATION CRITERION

Due to the difficulty of the multidimensional integration appeared for the statistical evidence, several approximations for the evidence have been developed. The Bayesian Information Criteria (BIC) (Schwarz 1978) is a well-known approximation, but it is valid only for Gaussian-like posterior probabilities. The WBIC (Watanabe 2012) is a more generic and easily computable approximation, which is defined by

$$\mathrm{WBIC} = \frac{\int {\rm d}\Theta(-\ln\mathcal{L}(\Theta))\mathcal{L}(\Theta)^\beta\pi(\Theta)}{\int {\rm d}\Theta\mathcal{L}(\Theta)^\beta\pi(\Theta)}\,. \tag{D1}$$

Here, β is called the inverse temperature, with is given by $\beta = 1/\ln N$ with N being the number of samples. We can easily calculate the WBIC by MCMC sampling of $-\mathcal{L}(\Theta)^\beta\pi(\Theta)$. The WBIC gives a good approximation of the minus log-evidence (or the free energy in the statistics) even for singular statistical models, such as the GMM. Our spectroscopic likelihood function contains the GMM, namely the foreground model, hence we adopt the WBIC to approximate the evidence.

APPENDIX E: PDFS OF SCULPTOR AND URSA MINOR

Here, we show the result of parameter estimation for Sculptor and Ursa Minor: Figs E1 and E2 are posterior PDFs, while Figs E3 and E4 are correlations between their J-factors and other parameters.

Downloaded from https://academic.oup.com/mnras/article/499/3/3320/5910521 by guest on 23 April 2024

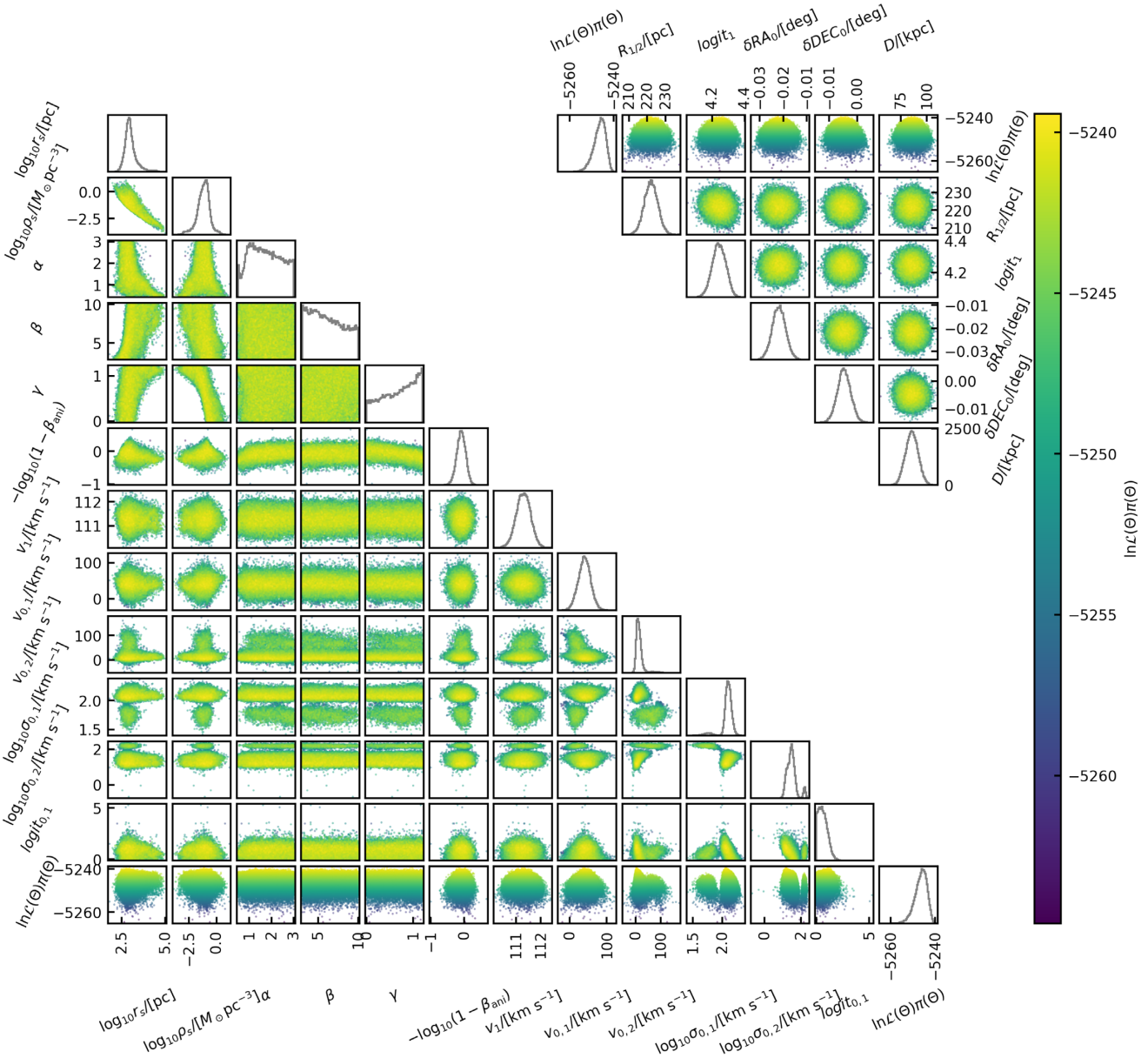

Figure E1. Posterior probability density and correlation matrix for the Sculptor. Multimodal distribution that we can see on the PDF is due to the fact that the contamination level of the dSph is very low (logit$_1 \sim 4.2$ or $s_{R_{1/2}} \sim 0.99$), so that the model cannot resolve foreground stars into two Gaussian distributions.

Downloaded from https://academic.oup.com/mnras/article/499/3/3320/5910521 by guest on 23 April 2024

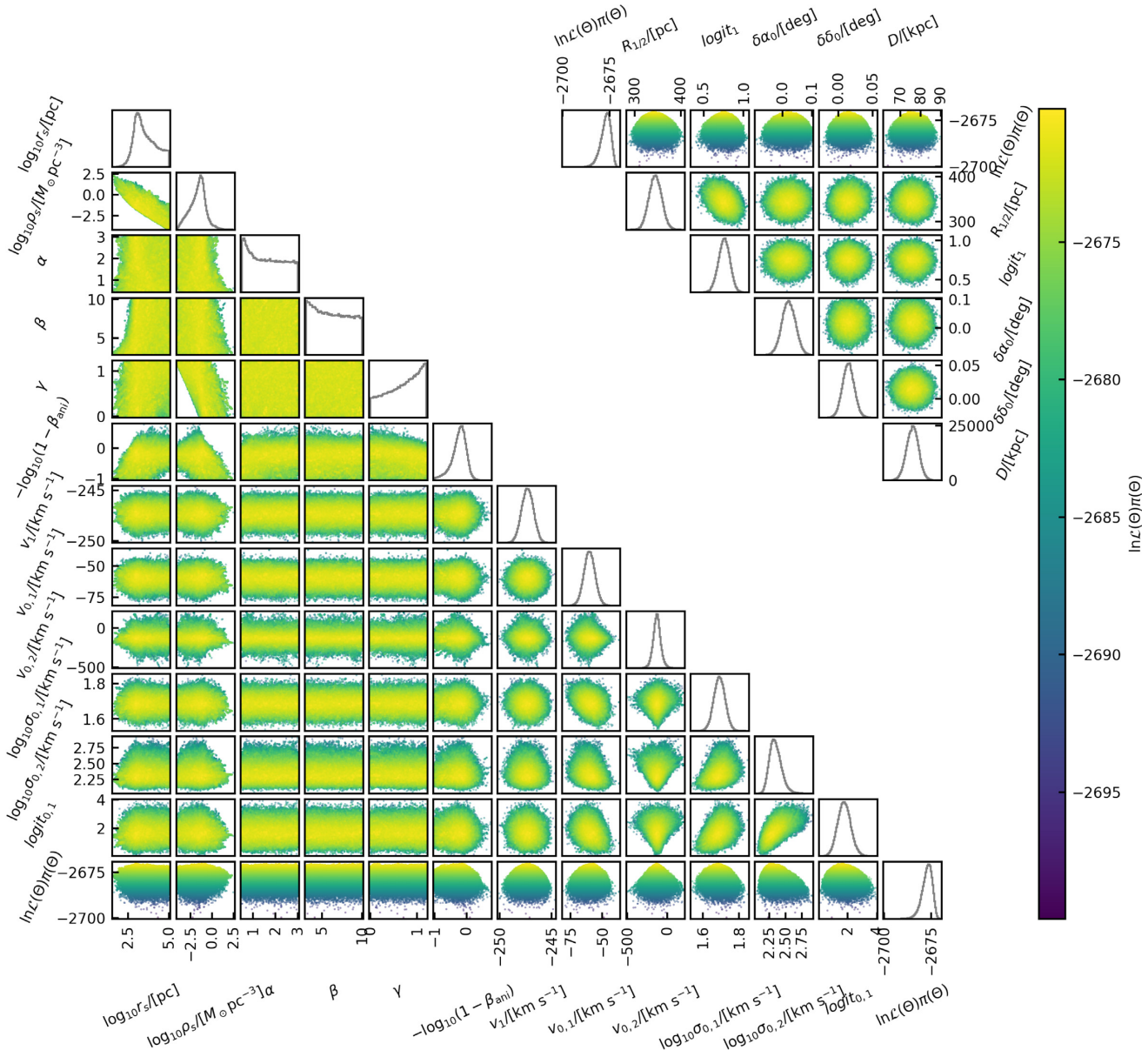

Figure E2. Posterior probability density and correlation matrix for the Ursa Minor.

Downloaded from https://academic.oup.com/mnras/article/499/3/3320/5910521 by guest on 23 April 2024

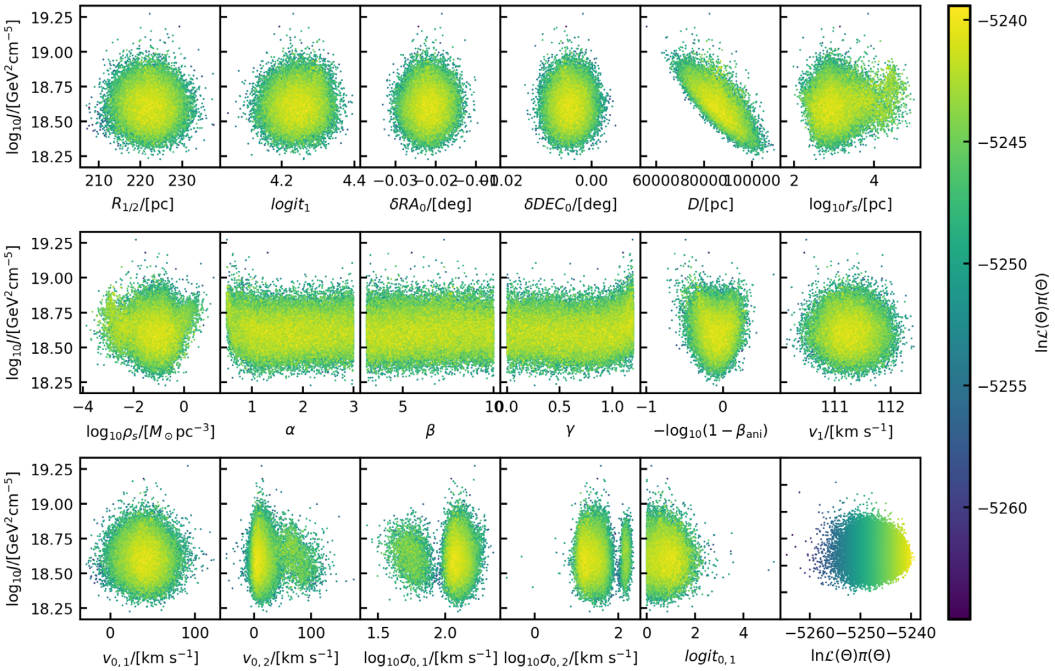

Figure E3. *J*-factor PDFs of the Sculptor dSph with respect to some other parameters.

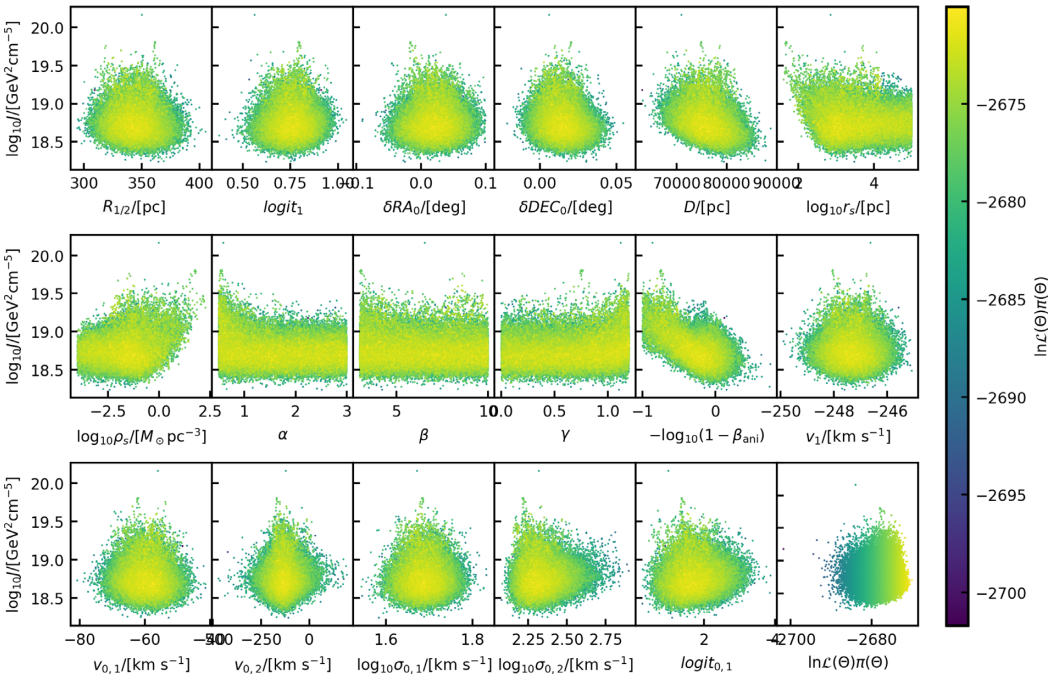

Figure E4. *J*-factor PDFs of the Ursa Minor dSph with respect to some other parameters.

Downloaded from https://academic.oup.com/mnras/article/499/3/3320/5910521 by guest on 23 April 2024

APPENDIX F: TRUNCATION

Dependence of the truncation radius $R_{\rm trunc}$ on the value of the *J*-factor for each dSph (Draco, Sculptor, Ursa Minor) is shown in Fig. F1. The radius that we used in our analysis is shown as a vertical dotted line. It can be seen that the value of the *J*-factor is not very sensitive to the choice of the truncation radius if it is large enough.

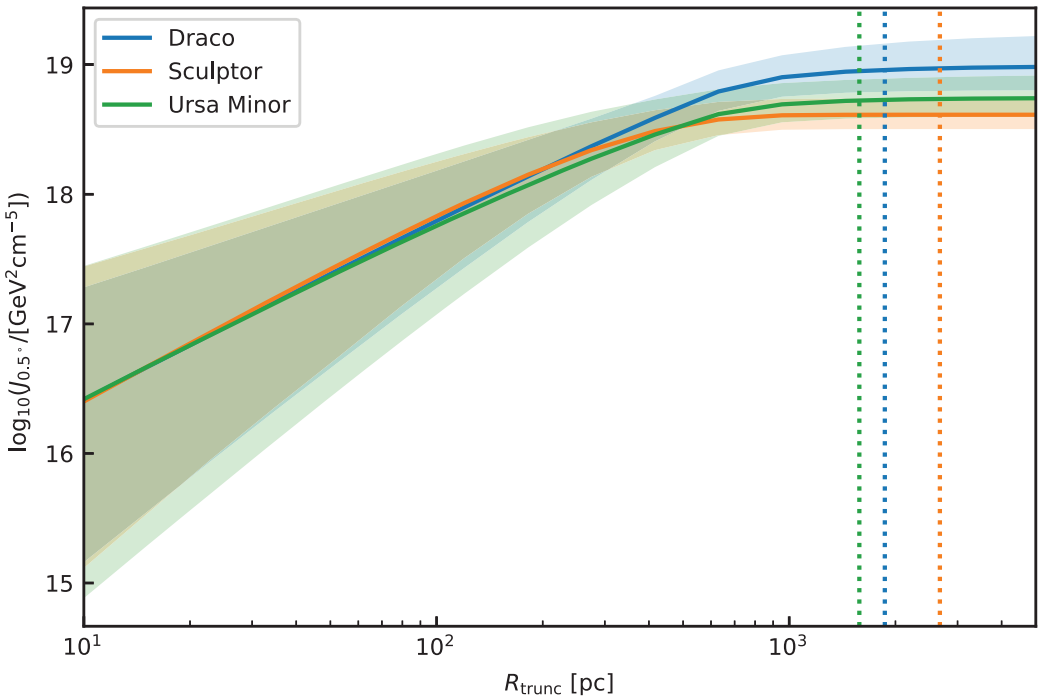

Figure F1. The value of the *J*-factor as a function of the truncation radius $R_{\rm trunc}$. The blue, orange, and green lines are the median values of *J*-factor for Draco, Sculptor, and Ursa Minor dSphs, respectively. On the other hand, the shaded area with the same colour code corresponds to the 68 per cent percentile of the Bayesian credible interval. The vertical dotted lines are the truncation radii that we used in our analysis, and exactly the same as those shown in Table 1.

This paper has been typeset from a TEX/LATEX file prepared by the author.

Downloaded from https://academic.oup.com/mnras/article/499/3/3320/5910521 by guest on 23 April 2024